

# On the origin of the BAOtr - DESI tension

Ioannis Pantos<sup>a</sup>, Leandros Perivolaropoulos<sup>a,\*</sup>

<sup>a</sup>*Department of Physics, University of Ioannina, GR-45110 Ioannina, Greece*

---

## Abstract

The fiducial-independent transversal BAO dataset (BAOtr) systematically prefers smaller comoving distance ratios  $D_M/r_d$  than the DESI DR2 three-dimensional BAO measurements at  $z \lesssim 0.65$ , driving dataset-dependent CPL dark-energy inferences and, consequently, conflicting conclusions about the Hubble tension. We investigate whether this disagreement can be attributed to the  $\Lambda$ CDM fiducial assumed in the 3D BAO pipeline, or resolved within the CPL dark-energy parametrisation. We show that the published 3D BAO distances are fiducial-independent by construction, with residual effects at  $\lesssim 0.3\%$  — negligible against the 10–18% BAOtr uncertainties. We then scan the CPL parameter space with  $\Omega_m$  and  $H_0$  jointly determined at each  $(w_0, w_a)$  by the Planck  $\theta_*$  constraint and optimisation against the DESI data. Two complementary tests are performed: a direct comparison of each DESI-optimized model with the BAOtr data, and an  $\alpha$ -interpolation test that anchors the prediction to the DESI measurements and asks whether the CPL backbone provides a better interpolation between them than  $\Lambda$ CDM. Both reveal an inescapable trade-off: models that fit DESI well ( $\chi_{\text{DESI}}^2 \lesssim 5$ ) yield  $\chi_{\text{BAOtr}}^2 \gtrsim 42$ , while reducing the BAOtr tension to  $\chi_{\text{BAOtr}}^2 \sim 37$  requires  $\chi_{\text{DESI}}^2 \gtrsim 8$ . No CMB-consistent CPL model fits both datasets simultaneously. The direct, model-independent comparison at  $z = 0.510$  — where BAOtr and DESI disagree by  $3.7\sigma$  (data-versus-data)— sets an irreducible tension floor that no smooth modification of  $D_M(z)$  can remove. These conclusions are robust across analysis methods, extrapolation schemes, and substitution of SDSS for DESI as the reference dataset. The remaining explanations are observational systematics — most plausibly in the angular BAO measurements — or new physics beyond CPL.

---

\*Corresponding author

*Email address:* leandros@uoi.gr (Leandros Perivolaropoulos)

*Keywords:* baryon acoustic oscillations, dark energy, cosmological tensions, fiducial cosmology, CPL parametrisation

---

## 1. Introduction

Baryon acoustic oscillations (BAO) imprint a characteristic comoving scale — the sound horizon at the baryon drag epoch,  $r_d \approx 147 \text{ Mpc}$  — on the matter distribution [1, 2, 3, 4, 5]. Observed as a peak in the galaxy two-point correlation function, this scale serves as a standard ruler that constrains the comoving angular diameter distance  $D_M(z)$  and the Hubble parameter  $H(z)$  across cosmic time. BAO measurements have matured from the first detections in SDSS [2] and 2dFGRS [6], through the BOSS and eBOSS programmes [7, 8], to the multi-tracer campaign of the Dark Energy Spectroscopic Instrument (DESI) [9, 10, 11]. The DESI second data release (DR2) [11], spanning  $0.1 < z < 4.2$  with seven tracer samples, reports a  $2.8\sigma$  preference for evolving dark energy in the Chevallier–Polarski–Linder (CPL) parametrisation [12, 13],  $w(a) = w_0 + w_a(1 - a)$ , when combined with Planck CMB data and Pantheon+ supernovae [14] — strengthening the earlier  $2.5\sigma$  hint from DR1 [10]. This result has stimulated extensive follow-up analyses exploring its robustness and physical implications [15, 16, 17, 18], adding to the broad literature on cosmological tensions [19, 20, 21].

A critical examination of the dataset dependence of this preference has been carried out by Xu et al. [22], who combine CMB anisotropies and lensing with four suites of late-time probes: DESI DR2 BAO, the SDSS-IV consensus [8], a transverse/angular BAO compilation (BAOtr) [23], and the Cepheid-calibrated PantheonPlus supernovae (PP&SH0ES) [24, 25, 26]. Their central finding is that the CPL inferences are strongly dataset-dependent: combinations involving 3D BAO (DESI or SDSS) prefer low  $H_0$  and a distinctive  $(w_0, w_a)$  locus, while combinations involving BAOtr and/or PP&SH0ES shift toward higher  $H_0$  and a different CPL region. The origin of this bifurcation is traced to a specific observational disagreement: the BAOtr dataset systematically prefers *smaller*  $D_M/r_d$  than the DESI DR2 measurements at all overlapping redshifts  $z \lesssim 0.65$ , with offsets of 10–13% at individual points. This low-redshift mismatch propagates through the CPL parameter space and is identified as the root cause of the divergent late-time reconstructions.

The BAOtr–BAO 3D disagreement is of particular significance because the two measurement approaches differ fundamentally in their relationship

to the assumed cosmological model. Standard 3D BAO analyses require a *fiducial cosmology* to convert observed angular separations and redshift differences into comoving distances, to apply the Alcock–Paczyński (AP) correction [27], and to construct the template correlation function against which the dilation parameters  $\alpha_{\perp}$  and  $\alpha_{\parallel}$  are measured. Both DESI DR2 and the SDSS-IV consensus adopt a Planck  $\Lambda$ CDM fiducial ( $\Omega_m = 0.3153$ ,  $H_0 = 67.36 \text{ km s}^{-1} \text{ Mpc}^{-1}$ ,  $r_d^{\text{fid}} = 147.05 \text{ Mpc}$ ). By contrast, BAOtr measurements [23, 28, 29, 30, 31, 32, 33] extract the angular BAO scale  $\theta_{\text{BAO}}(z) = r_d/D_M(z)$  from the two-point angular correlation function  $w(\theta)$  in thin redshift shells, without any conversion to comoving coordinates. The BAOtr observable is therefore fiducial-independent by construction. This methodological asymmetry raises a natural question: could the BAOtr–BAO 3D tension be a consequence of the  $\Lambda$ CDM fiducial assumed in the 3D analyses?

Three logically distinct classes of explanation exist for the observed tension:

1. **Fiducial misspecification.** The  $\Lambda$ CDM fiducial biases the published 3D BAO distances, and BAOtr reveals this bias. Adopting a CPL fiducial would reduce the disagreement.
2. **Observational systematics.** Unidentified systematic effects in one or both methodologies — projection effects, photometric-redshift uncertainties, or angular-mask artefacts in BAOtr; residual template mismatch or reconstruction biases in 3D BAO — produce a coherent offset.
3. **New physics.** The true distance–redshift relation differs from both  $\Lambda$ CDM and CPL in ways that the two-parameter CPL ansatz cannot capture. Models with richer late-time dynamics — such as  $\Lambda_s$ CDM [34, 35, 36], omnipotent dark energy [37], phantom-crossing scenarios [38, 39], or braneworld models [40] — might provide a better description.

In this paper we focus on hypothesis (i) and test whether the CPL parametrisation can reconcile the two BAO datasets. Our analysis proceeds in two stages. First, we show that the published 3D BAO distance ratios  $D_M/r_d$  are fiducial-independent as a direct consequence of the definition of the dilation parameters: the fiducial dependence of  $\alpha_{\perp}$  cancels identically against that of  $D_M^{\text{fid}}/r_d^{\text{fid}}$  in the published product. Residual effects (AP peak distortion, reconstruction sensitivity, broadband-polynomial incompleteness) have been quantified by the DESI collaboration at  $\lesssim 0.1\text{--}0.3\%$  [11, 41] — negligible compared to the 10–18% BAOtr uncertainties. A “rescaling” approach that multiplies published distances by the ratio  $\mathcal{R}_{\perp} = D_M^{\text{CPL}}/D_M^{\Lambda\text{CDM}}$

therefore overcorrects by a factor of 20–50. Second, we scan the CPL parameter space with  $\Omega_m$  adjusted at each  $(w_0, w_a)$  to satisfy the Planck angular scale constraint  $\theta_*$ , and compare each CMB-consistent model with both the DESI and BAOtr data. We find that no CPL model fits both datasets simultaneously: the  $\chi_{\text{DESI}}^2$  vs  $\chi_{\text{BAOtr}}^2$  trade-off traces an anti-correlation across the entire parameter space, with no model reaching the lower-left (good-fit) corner. The direct comparison at  $z = 0.510$  — where BAOtr and DESI measure  $D_M/r_d$  at the same redshift and disagree by  $3.7\sigma$  (data-versus-data) — sets an irreducible floor that no smooth model change can remove. These results are confirmed by an independent  $\alpha$ -interpolation analysis that anchors predictions to the DESI data points, and are robust across extrapolation schemes, BGS anchor inclusion, and substitution of SDSS for DESI. The fiducial-misspecification hypothesis is therefore ruled out, and the CPL framework cannot reconcile the two BAO datasets. The remaining possibilities are observational systematics — most plausibly in the angular BAO measurements — or new physics beyond CPL. This is consistent with recent independent findings that BAO miscalibrations are unlikely to rescue late-time solutions to the Hubble tension [42].

The paper is organised as follows. Section 2 establishes the fiducial independence of published 3D BAO distances and diagnoses the rescaling over-correction. Section 3 presents the three BAO datasets. Section 4 describes the CPL models with CMB-consistent  $\Omega_m$  and the two tension statistics. Section 5 presents the baseline tension, the CPL scan, robustness tests, and the consistency between methods. Section 6 discusses the remaining explanations and the connection to the Hubble tension. Section 7 summarises our conclusions.

## 2. Fiducial independence of published BAO distances

### 2.1. The 3D BAO pipeline

The standard 3D BAO analysis pipeline, as implemented in both DESI [11] and SDSS/BOSS/eBOSS [7, 8], transforms raw galaxy positions into measurements of  $D_M/r_d$  and  $D_H/r_d$  through four steps, each with a distinct relationship to the assumed fiducial cosmology. We trace the fiducial dependence through each step and show that it cancels identically in the published product.

**Step 1: Coordinate conversion.** The observables for each galaxy pair — angular separation  $\Delta\theta$  and redshift difference  $\Delta z$  — are converted to

comoving separations using a fiducial cosmology:

$$s_{\perp} = D_{\text{M}}^{\text{fid}}(z) \cdot \Delta\theta, \quad s_{\parallel} = D_{\text{H}}^{\text{fid}}(z) \cdot \Delta z, \quad (1)$$

where  $D_{\text{H}}^{\text{fid}} \equiv c/H^{\text{fid}}(z)$ . Both DESI DR2 and SDSS-IV use the Planck 2018  $\Lambda$ CDM best fit ( $\Omega_m = 0.3153$ ,  $H_0 = 67.36 \text{ km s}^{-1} \text{ Mpc}^{-1}$ ,  $r_{\text{d}}^{\text{fid}} = 147.05 \text{ Mpc}$ ) [14]. If the fiducial does not match the true cosmology, this mapping introduces the Alcock–Paczyński (AP) distortion [27]: an anisotropic, smooth, scale-independent rescaling of the clustering pattern.

**Step 2: Correlation function and reconstruction.** The pipeline computes the anisotropic two-point correlation function  $\xi(s_{\perp}, s_{\parallel})$  using the Landy–Szalay estimator [43], typically after a reconstruction procedure [44, 45] that partially reverses non-linear displacements and sharpens the BAO peak. Because the coordinate conversion uses fiducial rather than true distances, the BAO ring appears not at  $s = r_{\text{d}}$  but at

$$s_{\text{BAO}}^{\perp} = D_{\text{M}}^{\text{fid}}(z) \cdot \frac{r_{\text{d}}}{D_{\text{M}}^{\text{true}}(z)}, \quad s_{\text{BAO}}^{\parallel} = D_{\text{H}}^{\text{fid}}(z) \cdot \frac{r_{\text{d}}}{D_{\text{H}}^{\text{true}}(z)}. \quad (2)$$

**Step 3: Template fitting.** Because the fiducial cosmology generally differs from the true one, the observed peak position (Eq. 2) does not coincide with the template prediction. This mismatch is absorbed by two free dilation parameters,  $\alpha_{\perp}$  and  $\alpha_{\parallel}$ , that independently rescale the template coordinates in the transverse and line-of-sight directions. A parametric model is fitted to  $\xi$  [46, 47, 48, 49]:

$$\xi_{\text{model}}(s_{\perp}, s_{\parallel}) = B(s) \xi_{\text{template}}(\alpha_{\perp} s_{\perp}, \alpha_{\parallel} s_{\parallel}) + A(s), \quad (3)$$

where  $\xi_{\text{template}}$  is computed in the fiducial cosmology (BAO peak at  $s = r_{\text{d}}^{\text{fid}}$ ),  $\alpha_{\perp}$  and  $\alpha_{\parallel}$  are dilation parameters, and  $B(s)$  and  $A(s)$  are broadband nuisance functions — typically low-order polynomials in  $1/s$  — that absorb all smooth distortions of  $\xi$ , including the AP effect, galaxy-bias uncertainties, non-linear mode coupling, and window-function effects. These smooth terms cannot absorb a shift of the sharp BAO peak (width  $\sim 10\text{--}20 h^{-1} \text{ Mpc}$ ), so  $\alpha_{\perp}$  and  $\alpha_{\parallel}$  are determined by the peak position alone.

In the rescaled template, the peak appears where  $\alpha_{\perp} s_{\perp} = r_{\text{d}}^{\text{fid}}$ , i.e. at  $s_{\perp} = r_{\text{d}}^{\text{fid}}/\alpha_{\perp}$ . Matching to the data peak (Eq. 2) gives

$$\alpha_{\perp} = \frac{r_{\text{d}}^{\text{fid}} \cdot D_{\text{M}}^{\text{true}}(z)}{D_{\text{M}}^{\text{fid}}(z) \cdot r_{\text{d}}} = \frac{D_{\text{M}}^{\text{true}}(z)/r_{\text{d}}}{D_{\text{M}}^{\text{fid}}(z)/r_{\text{d}}^{\text{fid}}}, \quad (4)$$

the standard definition (Eq. (1) of Ref. [11]). Note the explicit fiducial dependence in the denominator. An analogous expression holds for  $\alpha_{\parallel}$ .

**Step 4: Published distances and the fiducial cancellation.** The pipeline reports

$$\left(\frac{D_M}{r_d}\right)^{\text{pub}} = \alpha_{\perp} \cdot \frac{D_M^{\text{fid}}}{r_d^{\text{fid}}}. \quad (5)$$

Substituting Eq. (4):

$$\left(\frac{D_M}{r_d}\right)^{\text{pub}} = \frac{D_M^{\text{true}}/r_d}{D_M^{\text{fid}}/r_d^{\text{fid}}} \cdot \frac{D_M^{\text{fid}}}{r_d^{\text{fid}}} = \frac{D_M^{\text{true}}}{r_d}. \quad (6)$$

The fiducial dependence of  $\alpha_{\perp}$  (the denominator in Eq. 4) cancels identically against the prefactor  $D_M^{\text{fid}}/r_d^{\text{fid}}$  in Eq. (5), leaving a result that depends only on the true cosmology. This cancellation is a direct algebraic consequence of the definition of  $\alpha_{\perp}$  and holds for *any* pair of fiducial cosmologies sharing the same  $r_d$ . It extends straightforwardly to the radial distance  $(D_H/r_d)^{\text{pub}}$  and to the isotropic combination  $(D_V/r_d)^{\text{pub}}$ . For models that change  $r_d$  (e.g., early dark energy [50, 51]), the published ratio still equals  $D_M^{\text{true}}/r_d$ ; the fiducial  $r_d^{\text{fid}}$  cancels regardless of whether it matches the true value.

As a numerical illustration, the DESI LRG1 measurement at  $z_{\text{eff}} = 0.510$  gives  $(D_M/r_d)^{\text{pub}} = 13.588 \pm 0.167$ . Switching the fiducial from Planck  $\Lambda$ CDM to the CPL model  $(w_0, w_a) = (-0.42, -1.75)$  changes  $\alpha_{\perp}$  by +6.3% and  $D_M^{\text{fid}}/r_d^{\text{fid}}$  by -5.9%; the two shifts cancel exactly in the product, which remains 13.588.

**Residual effects.** The cancellation of Eq. (6) is exact within the idealised fitting model of Eq. (3). In practice, three effects introduce a residual fiducial sensitivity: (i) anisotropic distortion of the BAO peak shape from the AP effect, which the isotropic broadband polynomials cannot fully absorb; (ii) sub-optimal reconstruction under a misspecified fiducial, leaving slightly larger non-linear broadening; and (iii) broadband-polynomial incompleteness at finite truncation order. The DESI collaboration has quantified all three through mock-catalogue tests with deliberately misspecified fiducials [11, 52, 41], finding a net residual bias  $\delta\alpha/\alpha \lesssim 0.1\text{--}0.3\%$  for fiducials within  $\sim 5\%$  of the truth. At  $z = 0.5$ , this corresponds to a bias in  $D_M/r_d$  of at most  $\sim 0.04$  units, compared to BAOtr uncertainties of  $\sigma \approx 0.4\text{--}0.9$  units. A detailed characterisation of these residual effects — including their dependence on the degree of fiducial mismatch and on the broadband parametrisation

— is beyond the scope of this work but would be valuable for future high-precision angular BAO comparisons.

## 2.2. Why the rescaling approach overcorrects

A natural but incorrect approach to testing the fiducial hypothesis would multiply the published  $(D_M/r_d)^{\text{pub}}$  by the ratio  $\mathcal{R}_\perp(z) = D_M^{\text{CPL}}(z)/D_M^{\Lambda\text{CDM}}(z)$  to “correct” for the  $\Lambda\text{CDM}$  fiducial. Since  $(D_M/r_d)^{\text{pub}} = D_M^{\text{true}}/r_d$  is already fiducial-independent (Eq. 6), this produces

$$\left(\frac{D_M}{r_d}\right)_{\text{rescaled}} = \frac{D_M^{\text{true}}}{r_d} \times \mathcal{R}_\perp(z), \quad (7)$$

which is the true distance multiplied by a spurious model-dependent factor. For the CPL models preferred by DESI+CMB analyses ( $w_0 > -1$ ,  $w_a < 0$ ),  $\mathcal{R}_\perp < 1$  at  $z \lesssim 1$ , so the rescaling systematically *shrinks* the DESI predictions — moving them toward BAOtr and producing an artificial tension reduction of  $\Delta\chi^2 \sim 40\text{--}50$ . Table 1 quantifies this overcorrection.

Table 1: Overcorrection from the rescaling approach at representative DESI redshifts, using the CMB+DESI CPL model ( $w_0 = -0.42$ ,  $w_a = -1.75$ ) [22]. The applied shift (3–6%) exceeds the mock-validated residual fiducial bias ( $\lesssim 0.3\%$ ) by a factor of 20–50.  $\mathcal{R}_\perp(z) = D_M^{\text{CPL}}(z)/D_M^{\Lambda\text{CDM}}(z)$  is evaluated numerically at each redshift using the stated CPL parameters with Planck 2018 background values ( $\Omega_m = 0.3153$ ,  $H_0 = 67.36 \text{ km s}^{-1} \text{ Mpc}^{-1}$ ).

$z$	$(D_M/r_d)^{\text{pub}}$	$\mathcal{R}_\perp$	Rescaled	Shift (%)	True residual (%)	Overcorrection
0.295	7.942 <sup>a</sup>	0.942	7.482	−5.8	$\lesssim 0.3$	$\gtrsim 19\times$
0.510	13.588	0.941	12.791	−5.9	$\lesssim 0.3$	$\gtrsim 20\times$
0.706	17.351	0.941	16.334	−5.9	$\lesssim 0.2$	$\gtrsim 29\times$
0.934	21.576	0.945	20.398	−5.5	$\lesssim 0.2$	$\gtrsim 27\times$
1.321	27.601	0.954	26.337	−4.6	$\lesssim 0.1$	$\gtrsim 46\times$
2.330	38.988	0.969	37.794	−3.1	$\lesssim 0.1$	$\gtrsim 31\times$

<sup>a</sup>BGS  $D_V/r_d$ ;  $\mathcal{R}_\perp$  here denotes  $\mathcal{R}_V = D_V^{\text{CPL}}/D_V^{\Lambda\text{CDM}}$ . The  $\lesssim 0.3\%$  residual is validated by DESI mock tests for both anisotropic and isotropic fits [11, 41].

A useful diagnostic for any analysis claiming to correct 3D BAO distances for fiducial effects: if the applied correction  $|f(z) - 1| \times 100\%$  exceeds the mock-validated residual ( $\lesssim 0.3\%$ ) by orders of magnitude, it is almost certainly overcorrecting. The correct procedure is not to modify the published  $D_M/r_d$  (which are fiducial-independent measurements of the true distance), but to change the cosmological model used to *predict*  $D_M/r_d$  and compare that prediction with both datasets — the approach we adopt in Section 4.

### 2.3. Angular BAO: fiducial-free by construction

The transversal (angular) BAO method extracts the BAO scale from the two-point angular correlation function  $w(\theta)$  of galaxies in thin, disjoint redshift shells [28, 53, 54]. Within each shell,  $w(\theta)$  is computed from angular pair counts using the Landy–Szalay estimator [43]; the BAO peak position  $\theta_{\text{BAO}}$  is identified by fitting a template to  $w(\theta)$  [28, 29, 30]. No fiducial cosmology enters at any stage: the pair separation is a directly observed angle, and the conversion to comoving distance,

$$\frac{D_{\text{M}}(z)}{r_{\text{d}}} = \frac{180^\circ/\pi}{\theta_{\text{BAO}}(z)}, \quad (8)$$

is exact for a flat universe and requires no assumed parameters.

The BAOtr compilation used in this work [23] assembles 15 measurements from four analyses of SDSS data (DR7–DR12): one low-redshift point from blue galaxies [31] ( $z = 0.110$ ), two from photometric LRGs [32] ( $z = 0.235, 0.365$ ), eleven from spectroscopic LRGs [29, 30] ( $z = 0.450\text{--}0.650$ ), and one from photometric quasars [33] ( $z = 2.225$ ). The measurements span  $0.110 \leq z \leq 2.225$  with the densest coverage at  $0.45 \lesssim z \lesssim 0.65$ , and are statistically independent by construction (disjoint shells).

Several systematic effects limit the precision of angular BAO and could contribute to the observed tension. Projection effects from finite shell width ( $\Delta z = 0.02\text{--}0.04$ ) can shift  $\theta_{\text{BAO}}$  at the  $\sim 0.5\text{--}1\%$  level [28, 55, 56]. Photometric redshift errors ( $\sigma_z/(1+z) \sim 0.02\text{--}0.04$ ) broaden the effective shell and amplify projection biases [57, 58]. All 15 measurements share the SDSS imaging footprint and its angular systematics (seeing, Galactic extinction, stellar contamination) [58, 59, 60], so a coherent angular systematic would bias all redshift bins in the same direction — mimicking a cosmological signal. These effects have not been characterised at the sub-percent level required by current 3D BAO comparisons, and we return to them in Section 6.2.

## 3. Data

### 3.1. DESI DR2 BAO

The DESI DR2 BAO measurements [11] are listed in Table 2. We use the 13 independent measurements from seven tracer samples spanning  $0.295 \leq z_{\text{eff}} \leq 2.330$ . The BGS sample at  $z_{\text{eff}} = 0.295$  provides only the isotropic distance  $D_{\text{V}}/r_{\text{d}} = 7.942 \pm 0.075$ ; the remaining six tracers provide both

$D_M/r_d$  and  $D_H/r_d$ . For the BAOtr comparison, which constrains only  $D_M/r_d$ , the six anisotropic  $D_M/r_d$  values (rows 2, 4, 6, 8, 10, 12) serve as anchor points, with the BGS measurement entering directly as a  $D_V/r_d$  constraint. Fractional uncertainties on  $D_M/r_d$  range from 0.7% (LRG3+ELG1) to 2.5% (QSO), making the DESI values 3–15 times more precise than BAOtr at comparable redshifts. As established in Section 2.1, all values are fiducial-independent.

Table 2: DESI DR2 BAO distance measurements [11]: 13 independent measurements from seven tracers. Distances are in units of  $r_d$ . The correlation coefficient  $\rho_{M,H} \equiv \rho(D_M/r_d, D_H/r_d)$  is listed for anisotropic tracers. Fiducial:  $r_d^{\text{fid}} = 147.05$  Mpc.

#	Tracer	$z$ -range	$z_{\text{eff}}$	Observable	Value $\pm \sigma$	$\rho_{M,H}$	Type
1	BGS	0.1–0.4	0.295	$D_V/r_d$	$7.942 \pm 0.075$	—	Bright galaxies
2	LRG1	0.4–0.6	0.510	$D_M/r_d$	$13.588 \pm 0.167$	−0.459	Lum. red galaxies
3	LRG1	0.4–0.6	0.510	$D_H/r_d$	$21.863 \pm 0.425$		
4	LRG2	0.6–0.8	0.706	$D_M/r_d$	$17.351 \pm 0.177$	−0.404	Lum. red galaxies
5	LRG2	0.6–0.8	0.706	$D_H/r_d$	$19.455 \pm 0.330$		
6	LRG3+ELG1	0.8–1.1	0.934	$D_M/r_d$	$21.576 \pm 0.152$	−0.416	LRGs + ELGs
7	LRG3+ELG1	0.8–1.1	0.934	$D_H/r_d$	$17.641 \pm 0.193$		
8	ELG2	1.1–1.6	1.321	$D_M/r_d$	$27.601 \pm 0.318$	−0.434	Emission-line gal.
9	ELG2	1.1–1.6	1.321	$D_H/r_d$	$14.176 \pm 0.221$		
10	QSO	0.8–2.1	1.484	$D_M/r_d$	$30.512 \pm 0.760$	−0.500	Quasars
11	QSO	0.8–2.1	1.484	$D_H/r_d$	$12.817 \pm 0.516$		
12	Ly $\alpha$	1.8–4.2	2.330	$D_M/r_d$	$38.988 \pm 0.531$	−0.431	Ly $\alpha$ forest
13	Ly $\alpha$	1.8–4.2	2.330	$D_H/r_d$	$8.632 \pm 0.101$		

### 3.2. SDSS-IV consensus BAO

As a cross-check, we use the SDSS-IV (BOSS + eBOSS) consensus compilation [8], listed in Table 3. Five  $D_M/r_d$  measurements (marked  $\star$ ) span  $z_{\text{eff}} = 0.380$ –2.334. Compared to DESI, SDSS provides an additional anchor at  $z = 0.380$  within the critical tension region, but lacks a BGS-equivalent below  $z = 0.380$ . At overlapping redshifts the two surveys agree within 1.5–4.5%: at  $z = 0.510$ , SDSS gives  $13.36 \pm 0.21$  vs DESI  $13.588 \pm 0.167$  ( $0.85\sigma$ ); at  $z \approx 2.33$ , SDSS gives  $37.30 \pm 1.70$  vs DESI  $38.988 \pm 0.531$  ( $0.95\sigma$ ). This consistency confirms that the 3D BAO distance scale is robust across independent surveys. For the Ly $\alpha$  sector, we use the cross-correlation measurement (row 13) following standard practice [8, 22].

Table 3: SDSS-IV (BOSS + eBOSS) consensus BAO measurements [8]. Rows marked  $\star$  are the five  $D_M/r_d$  anchors used in our cross-check analysis.

#	Sample	$z_{\text{eff}}$	Observable	Value $\pm \sigma$	Note
1	MGs	0.150	$D_V/r_d$	$4.47 \pm 0.17$	Isotropic <sup>a</sup>
2 $\star$	BOSS Galaxy	0.380	$D_M/r_d$	$10.23 \pm 0.17$	<sup>b</sup>
3	BOSS Galaxy	0.380	$D_H/r_d$	$25.00 \pm 0.76$	<sup>b</sup>
4 $\star$	BOSS Galaxy	0.510	$D_M/r_d$	$13.36 \pm 0.21$	<sup>b</sup>
5	BOSS Galaxy	0.510	$D_H/r_d$	$22.33 \pm 0.58$	<sup>b</sup>
6 $\star$	eBOSS LRG	0.700	$D_M/r_d$	$17.86 \pm 0.33$	<sup>c,d</sup>
7	eBOSS LRG	0.700	$D_H/r_d$	$19.33 \pm 0.53$	<sup>c,d</sup>
8	eBOSS ELG	0.845	$D_V/r_d$	$18.33 \pm 0.62$	Isotropic <sup>e</sup>
9	eBOSS QSO	1.480	$D_H/r_d$	$13.26 \pm 0.55$	<sup>f,g</sup>
10 $\star$	eBOSS QSO	1.480	$D_M/r_d$	$30.69 \pm 0.80$	<sup>f,g</sup>
11	Ly $\alpha$ auto	2.330	$D_M/r_d$	$37.60 \pm 1.90$	Corr. w/ 13 <sup>h</sup>
12	Ly $\alpha$ auto	2.330	$D_H/r_d$	$8.93 \pm 0.28$	Corr. w/ 13 <sup>h</sup>
13 $\star$	Ly $\alpha$ ×QSO	2.334	$D_M/r_d$	$37.30 \pm 1.70$	Cross-corr. <sup>h</sup>
14	Ly $\alpha$ ×QSO	2.334	$D_H/r_d$	$9.08 \pm 0.34$	<sup>h</sup>

<sup>a</sup> [61]; <sup>b</sup> [7]; <sup>c</sup> [62]; <sup>d</sup> [63]; <sup>e</sup> [64]; <sup>f</sup> [65]; <sup>g</sup> [66]; <sup>h</sup> [67].

### 3.3. BAOtr compilation

Table 4 lists the 15 BAOtr measurements from Ref. [23], with derived  $D_M/r_d$  values computed via Eq. (8). Fractional uncertainties range from 2.5% ( $z = 0.235$ ) to 17.5% ( $z = 2.225$ ), roughly an order of magnitude larger than the DESI measurements at comparable redshifts. The data show non-monotonic scatter in  $D_M/r_d$  at  $z = 0.45$ – $0.65$  (e.g.,  $D_M/r_d$  drops from 12.01 at  $z = 0.450$  to 11.41 at  $z = 0.470$ ), consistent with the 4–7% statistical uncertainties but cautioning against over-interpreting individual points. Only one BAOtr measurement exactly coincides with a DESI anchor: at  $z = 0.510$ , BAOtr gives  $D_M/r_d = 11.912 \pm 0.421$  while DESI gives  $13.588 \pm 0.167$  — a direct, interpolation-free difference of  $3.7\sigma$ . The 15 measurements are drawn from four distinct SDSS analyses using different galaxy selections and template-fitting methods, providing some protection against a single analysis-specific bias, but all share the SDSS imaging footprint and its angular systematics.

### 3.4. The BAOtr–BAO 3D tension

Xu et al. [22] identify a systematic offset: BAOtr prefers smaller  $D_M/r_d$  than DESI at all overlapping redshifts  $z \lesssim 0.65$ , with the discrepancy most

Table 4: Transversal (angular) BAO measurements [23].  $\theta_{\text{BAO}}(z) = r_d/D_M(z)$  is measured from  $w(\theta)$  without a fiducial cosmology. Derived  $D_M/r_d$  values follow from Eq. (8).

#	$z$	$\theta_{\text{BAO}}$ [deg]	$\sigma_\theta$ [deg]	$D_M/r_d$	$\sigma_{D_M/r_d}$	Source	$\sigma_\theta/\theta_{\text{BAO}}$
1	0.110	19.80	3.26	2.894	0.477	[31] <sup>a</sup>	16.5%
2	0.235	9.06	0.23	6.324	0.161	[32] <sup>b</sup>	2.5%
3	0.365	6.33	0.22	9.052	0.315	[32] <sup>b</sup>	3.5%
4	0.450	4.77	0.17	12.012	0.428	[29] <sup>c</sup>	3.6%
5	0.470	5.02	0.25	11.414	0.568	[29] <sup>c</sup>	5.0%
6	0.490	4.99	0.21	11.483	0.483	[29] <sup>c</sup>	4.2%
7	0.510	4.81	0.17	11.912	0.421	[29] <sup>c</sup>	3.5%
8	0.530	4.29	0.30	13.356	0.934	[29] <sup>c</sup>	7.0%
9	0.550	4.25	0.25	13.481	0.793	[29] <sup>c</sup>	5.9%
10	0.570	4.62	0.40	12.402	1.074	[30] <sup>d</sup>	8.7%
11	0.590	4.37	0.35	13.111	1.050	[30] <sup>d</sup>	8.0%
12	0.610	3.86	0.33	14.843	1.269	[30] <sup>d</sup>	8.5%
13	0.630	3.88	0.42	14.767	1.598	[30] <sup>d</sup>	10.8%
14	0.650	3.54	0.17	16.185	0.777	[30] <sup>d</sup>	4.8%
15	2.225	1.77	0.31	32.371	5.667	[33] <sup>e</sup>	17.5%

<sup>a</sup> SDSS DR7 blue galaxies; <sup>b</sup> SDSS DR10/DR11 phot. LRGs; <sup>c</sup> SDSS DR10 LRGs;

<sup>d</sup> SDSS DR11 LRGs; <sup>e</sup> SDSS DR12 phot. quasars.

pronounced at  $z \approx 0.35$ – $0.55$  (individual offsets of  $\sim 10$ – $13\%$  in  $D_M/r_d$ , corresponding to  $2$ – $4\sigma$  per point). The same pattern is observed with SDSS replacing DESI. This low-redshift disagreement propagates into divergent CPL inferences: CMB + 3D BAO combinations drive the fit toward  $w_0 \approx -0.4$ ,  $w_a \approx -1.8$ , with  $H_0 \approx 64 \text{ km s}^{-1} \text{ Mpc}^{-1}$ , while CMB + BAOtr combinations prefer  $w_0 \approx -0.7$ ,  $w_a \approx -1.8$ , with  $H_0 \approx 71$ – $73 \text{ km s}^{-1} \text{ Mpc}^{-1}$  [22]. The Bayesian evidence for CPL over  $\Lambda$ CDM is very strong ( $\Delta \ln \mathcal{Z} \approx 16$ ) when BAOtr and PP&SH0ES are included, but inconclusive for CMB+DESI and moderately favouring  $\Lambda$ CDM for CMB+SDSS. The tension is thus directly connected to the Hubble tension: BAOtr-inclusive combinations yield  $H_0$  consistent with local measurements [68], while 3D-BAO-inclusive combinations worsen the discrepancy.

As shown in Section 2.1, the fiducial cosmology cannot explain this disagreement: the published 3D BAO distances depend on the fiducial at the  $\lesssim 0.3\%$  level, two orders of magnitude below the observed offsets. The three hypotheses of Section 1 therefore reduce to two: observational systematics or new physics.

## 4. Method

### 4.1. CPL dark energy and CMB-consistent parameters

We adopt the CPL parametrisation [12, 13] for the dark-energy equation of state,

$$w(a) = w_0 + w_a (1 - a), \quad (9)$$

where  $a = (1 + z)^{-1}$ . In a spatially flat universe with matter, radiation, and dark energy, the normalised Hubble rate is

$$E^2(z) = \Omega_m(1+z)^3 + \Omega_r(1+z)^4 + \Omega_{\text{DE}}(1+z)^{3(1+w_0+w_a)} \exp\left[-\frac{3w_a z}{1+z}\right], \quad (10)$$

with  $\Omega_{\text{DE}} = 1 - \Omega_m - \Omega_r$  and  $\Omega_r = \Omega_m/(1 + z_{\text{eq}})$ ,  $z_{\text{eq}} = 3387$  [14]. The three distance measures relevant for BAO are the comoving distance

$$D_{\text{M}}(z) = \frac{c}{H_0} \int_0^z \frac{dz'}{E(z')}, \quad (11)$$

the Hubble distance  $D_{\text{H}}(z) = c/[H_0 E(z)]$ , and the volume-averaged distance  $D_{\text{V}}(z) = [z D_{\text{M}}(z)^2 D_{\text{H}}(z)]^{1/3}$ . All are reported in units of  $r_{\text{d}}$ , so the dependence on  $H_0$  partially cancels but does not vanish:  $D_{\text{M}}/r_{\text{d}} = (c/H_0 r_{\text{d}}) \int_0^z dz'/E(z')$  depends on  $H_0$  through the prefactor  $c/(H_0 r_{\text{d}})$ .

*CMB-consistent* ( $\Omega_m, H_0$ ) at each  $(w_0, w_a)$

We fix  $r_{\text{d}} = 147.09$  Mpc [14] and determine both  $\Omega_m$  and  $H_0$  from two constraints: the Planck angular scale  $\theta_*$  and the best fit to the DESI data.

The primary CMB geometric observable is  $\theta_* = r_*/D_{\text{M}}(z_*)$ , measured with fractional precision 0.030% [14]. Since CPL modifies only the post-recombination expansion,  $r_*$  is unchanged and the constraint fixes  $D_{\text{M}}(z_*)$ . Writing  $D_{\text{M}}(z_*) = (c/H_0) \int_0^{z_*} dz'/E(z'; \Omega_m, w_0, w_a)$ , the  $\theta_*$  constraint determines  $H_0$  as a function of  $\Omega_m$  at each  $(w_0, w_a)$ :

$$H_0(\Omega_m, w_0, w_a) = H_0^{\text{Planck}} \frac{\int_0^{z_*} dz'/E(z'; \Omega_m, w_0, w_a)}{\int_0^{z_*} dz'/E(z'; \Omega_m^{\text{Planck}}, -1, 0)}, \quad (12)$$

where  $H_0^{\text{Planck}} = 67.36 \text{ km s}^{-1} \text{ Mpc}^{-1}$  and  $\Omega_m^{\text{Planck}} = 0.3153$ . This ensures  $D_{\text{M}}(z_*) = D_{\text{M}}^{\text{ACDM}}(z_*)$  by construction, so that  $\theta_*$  matches the Planck measurement.

With  $H_0(\Omega_m)$  fixed by Eq. (12), the remaining free parameter  $\Omega_m$  is determined by minimising the DESI  $\chi^2$ :

$$\Omega_m^{\text{best}}(w_0, w_a) = \arg \min_{\Omega_m} \chi_{\text{DESI}}^2(\Omega_m, H_0(\Omega_m), w_0, w_a). \quad (13)$$

This is a one-dimensional minimisation at each grid point, solved numerically over  $0.15 < \Omega_m < 0.55$ . The procedure yields, at each  $(w_0, w_a)$ , the CMB-consistent CPL model that *best represents the DESI data*, enabling a fair comparison with BAOtr: we ask whether the model that optimally describes DESI also describes BAOtr.

We note that matching  $\theta_*$  alone does not guarantee consistency with the full CMB power spectrum; models with extreme  $(w_0, w_a)$  may require  $\Omega_m$  or  $H_0$  values that conflict with the CMB peak structure. A full MCMC with Planck likelihoods would be needed to assess this, but the geometric constraint captures the dominant degeneracy.<sup>1</sup>

Table 5 lists the DESI-optimized parameters at the published CPL posterior centres. The CMB+DESI model recovers  $\Omega_m = 0.352$ ,  $H_0 = 63.8 \text{ km s}^{-1} \text{ Mpc}^{-1}$  — consistent with the Xu et al. posterior ( $\Omega_m \approx 0.350$ ,  $H_0 \approx 63.9$ ), confirming that our procedure captures the correct parameter degeneracy.

Table 5: DESI-optimized parameters at each  $(w_0, w_a)$ :  $\Omega_m$  minimises  $\chi_{\text{DESI}}^2$  with  $H_0$  set by the  $\theta_*$  constraint (Eq. 12). Our values are deterministic at fixed  $(w_0, w_a)$ ; the Xu et al. column shows marginalised posteriors from full MCMC fits [22]. The two differ because the MCMC also adjusts  $\Omega_b h^2$  and  $n_s$ .

Model	$w_0$	$w_a$	$\Omega_m$	$H_0$	$\Omega_m^{\text{Xu}}$ (Xu et al.)	$H_0^{\text{Xu}}$
$\Lambda$ CDM	-1.000	0.000	0.299	68.8	$0.3153 \pm 0.0073$	$67.36 \pm 0.54$
CMB+PP&SH0ES	-0.694	-1.700	0.318	67.7	$0.283 \pm 0.006$	—
CMB+PP&SH0ES+BAOtr	-0.660	-1.910	0.319	67.6	$0.279 \pm 0.006$	—
CMB+SDSS	-0.480	-1.510	0.347	64.1	$0.355 \pm 0.026$	$63.6^{+2.2}_{-2.5}$
CMB+DESI	-0.420	-1.750	0.352	63.8	$0.350 \pm 0.021$	$63.9 \pm 2.0$

<sup>1</sup>The small difference between our  $\Omega_m^{\text{best}}$  and the marginalised values of Xu et al. [22] arises because their MCMC also adjusts  $\Omega_b h^2$  and  $n_s$  to fit the full CMB spectrum, not just  $\theta_*$ .

*Parameter space and prior*

We scan

$$w_0 \in [-2.5, 0.5], \quad w_a \in [-5.5, 2.5], \quad (14)$$

subject to  $w_0 + w_a < 0$  (early-matter-domination prior). At each grid point,  $\Omega_m$  and  $H_0$  are determined by Eqs. (12)–(13), so the scan explores the one-dimensional DESI-optimized, CMB-consistent subspace at each  $(w_0, w_a)$ .

*4.2. Tension statistic*

We quantify the BAOtr–BAO 3D tension using two complementary methods. Method A (direct model comparison) serves as the primary analysis; Method B ( $\alpha$ -interpolation) provides an independent cross-check.

*Method A: direct model comparison (primary)*

At each  $(w_0, w_a)$  with DESI-optimized  $(\Omega_m, H_0)$ , we compute the model predictions and compare directly with both datasets:

$$\chi_{\text{BAOtr}}^2(w_0, w_a) = \sum_{i=1}^{15} \left[ \frac{(D_M/r_d)_i^{\text{BAOtr}} - (D_M/r_d)^{\mathcal{M}}(z_i)}{\sigma_{\text{BAOtr},i}} \right]^2, \quad (15)$$

$$\chi_{\text{DESI}}^2(w_0, w_a) = \sum_{j=1}^{N_{\text{anc}}} \left[ \frac{X_j^{\text{data}} - X_j^{\mathcal{M}}(z_j)}{\sigma_j} \right]^2, \quad (16)$$

In Eq. (16)  $X_j$  denotes  $D_M/r_d$  for the six anisotropic tracers and  $D_V/r_d$  for BGS.  $\chi_{\text{DESI}}^2$  is minimised at each  $(w_0, w_a)$ ; the question is whether the DESI-optimized model also fits BAOtr. The 15 BAOtr points are treated as independent (disjoint shells); we note that shared SDSS angular systematics could introduce correlated biases, effectively reducing the number of independent degrees of freedom (Section 6.4).

We scan on a  $55 \times 55$  grid over the range of Eq. (14).

*Method B:  $\alpha$ -interpolation (cross-check)*

Method A asks which model best fits each dataset. Method B asks a complementary question: *accepting the DESI data as fixed anchors*, does CPL provide a better interpolation between them than  $\Lambda$ CDM?

At each DESI anchor redshift  $z_j$ , we define

$$\alpha_j(w_0, w_a) = \frac{(D_M/r_d)_j^{\text{data}}}{(D_M/r_d)^{\mathcal{M}}(z_j)}, \quad (17)$$

using the DESI-optimized  $(\Omega_m, H_0)$ . For the BGS anchor,  $(D_M/r_d)^{\text{data}}$  is obtained from the measured  $D_V/r_d$  using the model-predicted  $D_H/r_d$ :  $D_M/r_d = [(D_V/r_d)^3/(z \cdot D_H^M/r_d)]^{1/2}$ . A continuous  $\alpha(z)$  is constructed by piecewise linear interpolation of  $\{z_j, \alpha_j\}$  in  $u = \ln(1+z)$ , with constant- $\alpha$  extrapolation below the lowest anchor (alternatives tested in Section 5.3). The predicted  $D_M/r_d$  at each BAOtr redshift is

$$\left(\frac{D_M}{r_d}\right)_i^{\text{pred}} = \alpha(z_i) \times \left(\frac{D_M}{r_d}\right)_i^{\mathcal{M}}, \quad (18)$$

and the tension statistic is

$$T_i = \frac{(D_M/r_d)_i^{\text{BAOtr}} - (D_M/r_d)_i^{\text{pred}}}{\sqrt{\sigma_{\text{BAOtr},i}^2 + \sigma_{\text{pred},i}^2}}, \quad \chi_B^2 = \sum_{i=1}^{15} T_i^2, \quad (19)$$

where  $\sigma_{\text{pred},i}$  propagates the DESI uncertainties through the interpolation (subdominant at all redshifts).

The key distinction: Method A allows the model to miss the DESI points and measures the absolute fit to each dataset. Method B forces the prediction through the DESI data (via  $\alpha$ -warping) and tests the *shape* between anchors. As we show in Section 5.4, both reach the same conclusion.

## 5. Results

### 5.1. Baseline tension under $\Lambda$ CDM

Table 6 presents the per-point BAOtr tension under the DESI-optimized  $\Lambda$ CDM model ( $\Omega_m = 0.299$ ,  $H_0 = 68.8 \text{ km s}^{-1} \text{ Mpc}^{-1}$ ,  $\chi_{\text{DESI}}^2 = 5.4$ ) for both methods.

Under Method A, the global tension is  $\chi_{\text{BAOtr}}^2 = 41.6$  for 15 points ( $p \approx 2 \times 10^{-4}$ ,  $3.5\sigma$ ), while the DESI fit is good ( $\chi_{\text{DESI}}^2 = 5.4$  for 7 points). Under Method B, the DESI-anchored prediction gives  $\chi_B^2 = 51.5$ , higher because the  $\alpha$ -warping amplifies the model–data offset at the anchor redshifts.

In Method A, all but one of the 15 tensions are negative; in Method B, all 15 are negative (BAOtr prefers smaller  $D_M/r_d$ ), and the tension is concentrated at  $z = 0.35$ – $0.60$ . The five points at  $z = 0.365$ ,  $0.470$ ,  $0.490$ ,  $0.510$ , and  $0.570$  contribute  $\chi^2 \approx 32$ – $35$  depending on method, accounting for  $\sim 78$ – $82\%$  of the total. The most significant point is  $z = 0.510$ , where the DESI-optimized  $\Lambda$ CDM prediction is  $D_M/r_d = 13.29$  while BAOtr gives

Table 6: Per-point BAOtr tension under the DESI-optimized  $\Lambda$ CDM model ( $\Omega_m = 0.299$ ,  $H_0 = 68.8 \text{ km s}^{-1} \text{ Mpc}^{-1}$ ).  $T_i^A$ : Method A (direct model);  $T_i^B$ : Method B ( $\alpha$ -interpolation with BGS anchor, constant- $\alpha$  extrapolation). Negative values indicate BAOtr prefers smaller  $D_M/r_d$ .

#	$z$	$(D_M/r_d)^{\text{BAOtr}}$	$\sigma$	Method A (direct)		Method B ( $\alpha$ )	
				$T_i^A$ [ $\sigma$ ]	$(\chi_i^2)^A$	$T_i^B$ [ $\sigma$ ]	$(\chi_i^2)^B$
1	0.110	2.894	0.477	-0.59	0.35	-0.61	0.38
2	0.235	6.324	0.161	-1.58	2.49	-1.50	2.25
3	0.365	9.052	0.315	-2.64	6.95	-2.82	7.93
4	0.450	12.012	0.428	+0.23	0.05	-0.25	0.06
5	0.470	11.414	0.568	-1.70	2.88	-2.06	4.25
6	0.490	11.483	0.483	-2.80	7.82	-3.21	10.30
7	0.510	11.912	0.421	-3.27	10.71	-3.70	13.70
8	0.530	13.356	0.934	-0.41	0.17	-0.68	0.47
9	0.550	13.481	0.793	-0.88	0.78	-1.15	1.33
10	0.570	12.402	1.074	-2.06	4.23	-2.23	4.96
11	0.590	13.111	1.050	-1.84	3.39	-1.98	3.92
12	0.610	14.843	1.269	-0.50	0.25	-0.59	0.34
13	0.630	14.767	1.598	-0.71	0.50	-0.75	0.56
14	0.650	16.185	0.777	-0.16	0.03	-0.20	0.04
15	2.225	32.371	5.667	-0.99	0.99	-1.01	1.02
<b>Total <math>\chi^2</math></b>				<b>41.6</b>		<b>51.5</b>	

$11.91 \pm 0.42$ , a  $3.3\sigma$  discrepancy contributing  $\chi^2 \approx 10.7$ . This per-point  $\chi^2$  contribution sets a robust floor on the BAOtr–DESI tension. The model-independent data-versus-data comparison at this redshift (Section 3.3) yields an even larger  $3.7\sigma$  clash, confirming that no smooth modification of  $D_M(z)$  can bring the two datasets into agreement.

Figure 1 displays the per-point tensions graphically.

## 5.2. No CMB-consistent CPL model resolves the tension

### The DESI–BAOtr trade-off

Figure 2 shows  $\chi_{\text{DESI}}^2$  vs  $\chi_{\text{BAOtr}}^2$  (Method A) for each DESI-optimized model in the scan. The anti-correlation is stark: no model falls in the lower-left corner. Among all models with  $\chi_{\text{DESI}}^2 < 20$  (622 models), the minimum  $\chi_{\text{BAOtr}}^2$  is 31.6. Among all models with  $\chi_{\text{DESI}}^2 < 15$ , the minimum  $\chi_{\text{BAOtr}}^2$  is 32.9. There are zero models with  $\chi_{\text{DESI}}^2 < 20$  and  $\chi_{\text{BAOtr}}^2 < 25$  simultaneously.

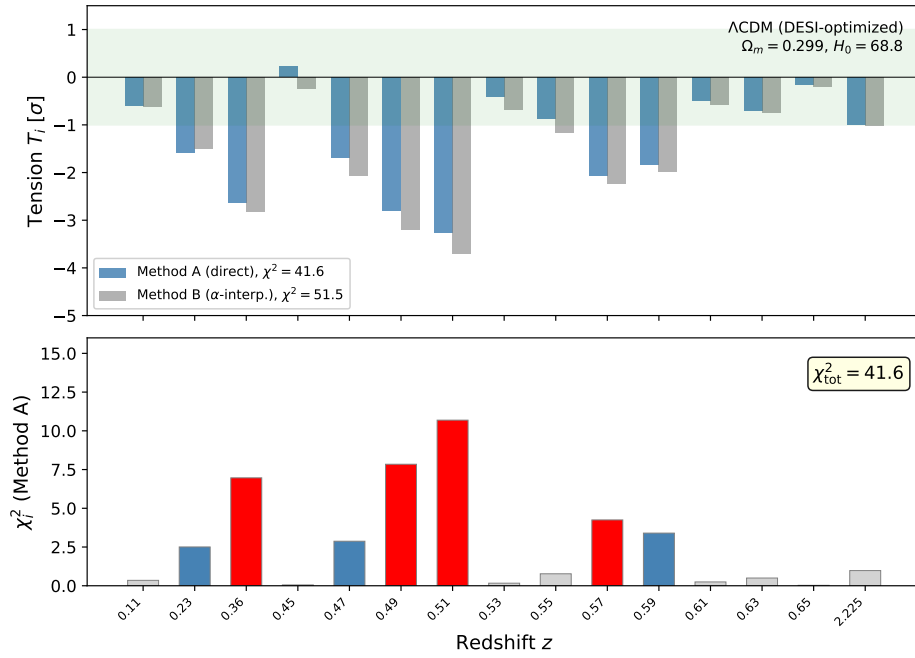


Figure 1: Per-redshift BAOtr tension under DESI-optimized  $\Lambda$ CDM ( $\Omega_m = 0.299$ ,  $H_0 = 68.8$ ). **Upper:** normalised tension  $T_i$ ; blue bars show Method A, grey bars Method B. The green band marks  $|T_i| < 1\sigma$ . **Lower:** per-point  $\chi_i^2$  (Method A). Red:  $\chi_i^2 > 4$ ; blue:  $1 < \chi_i^2 \leq 4$ ; grey:  $\chi_i^2 \leq 1$ .

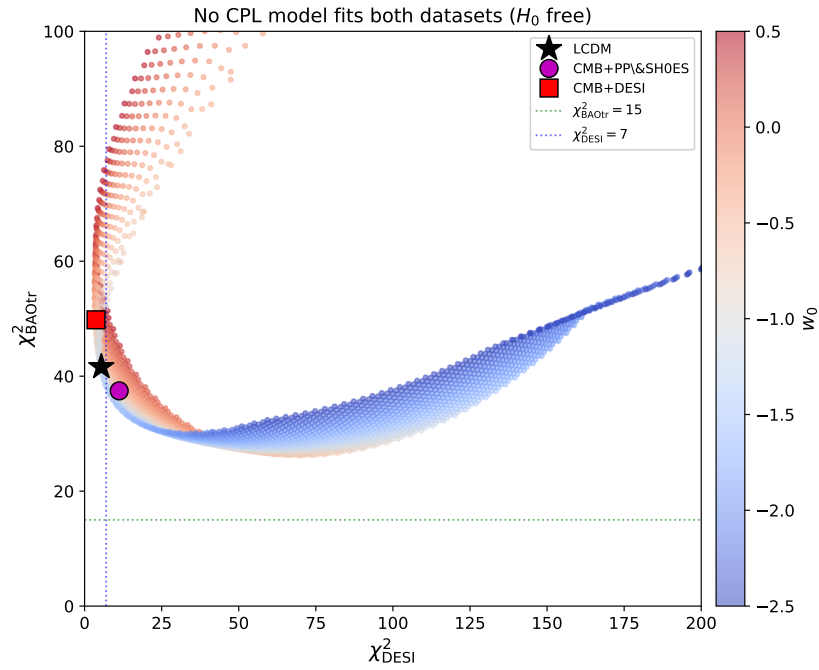


Figure 2: Trade-off between  $\chi^2_{\text{DESI}}$  and  $\chi^2_{\text{BAOtr}}$  (Method A) across the DESI-optimized, CMB-consistent CPL parameter space. Each point represents a  $(w_0, w_a)$  model with  $(\Omega_m, H_0)$  set by Eqs. (12)–(13), coloured by  $w_0$ . The black star marks  $\Lambda$ CDM; the magenta circle CMB+PP&SHOES; the red square CMB+DESI. Dotted lines show the expected  $\chi^2$  for consistency. No CPL model reaches the lower-left corner.

### $\chi^2$ summary

Table 7 presents the  $\chi^2$  values for both methods at the published CPL posteriors.

Table 7: Tension  $\chi^2$  for DESI-optimized CPL models under both methods.  $\Delta\chi^2 = \chi^2 - \chi_{\Lambda\text{CDM}}^2$ : positive values mean the BAOtr tension increases. Method A reports  $\chi_{\text{BAOtr}}^2$  and  $\chi_{\text{DESI}}^2$ ; Method B reports the DESI-anchored  $\chi_B^2$ .

Model	$w_0$	$w_a$	$\Omega_m$	$H_0$	Method A		Method B		
					$\chi_{\text{BAOtr}}^2$	$\chi_{\text{DESI}}^2$	$\chi_B^2$	$\Delta\chi_B^2$	
$\Lambda\text{CDM}$	-1.00	0.00	0.299	68.8	41.6	5.4	51.5	—	
<i>Published posteriors [22]:</i>									
CMB+PP&SH0ES	-0.69	-1.70	0.318	67.7	37.4	11.2	53.0	+1.5	
CMB+PP&SH0ES+BAOtr	-0.66	-1.91	0.319	67.6	36.9	12.5	53.2	+1.6	
CMB+SDSS	-0.48	-1.51	0.347	64.1	49.7	3.7	54.3	+2.8	
CMB+DESI	-0.42	-1.75	0.352	63.8	49.8	3.7	54.7	+3.2	

The two methods tell a consistent story:

1. **Method A:** The CMB+DESI CPL model fits DESI well ( $\chi_{\text{DESI}}^2 = 3.7$ ) but makes the BAOtr tension *worse* ( $\chi_{\text{BAOtr}}^2 = 49.8$ , up from 41.6 under  $\Lambda\text{CDM}$ ). This model has  $\Omega_m = 0.352$  and  $H_0 = 63.8 \text{ km s}^{-1} \text{ Mpc}^{-1}$ : the lower  $H_0$  increases  $D_M/r_d$  (since  $D_M \propto c/H_0$ ), pushing the prediction above BAOtr. Conversely, the CMB+PP&SH0ES model modestly improves the BAOtr fit ( $\chi_{\text{BAOtr}}^2 = 37.4$ ) but worsens the DESI fit ( $\chi_{\text{DESI}}^2 = 11.2$ ).
2. **Method B:** All published CPL posteriors *increase* the DESI-anchored tension ( $\Delta\chi_B^2 = +1.5$  to  $+3.2$ ). This occurs because CPL with  $w_0 > -1$  predicts smaller  $D_M/r_d$  than  $\Lambda\text{CDM}$  at the anchor redshifts (at matched  $H_0$ ), inflating  $\alpha_j$  above unity and pushing the interpolated prediction further from BAOtr.

### $\chi^2$ surfaces

Figure 3 shows the  $\chi_{\text{BAOtr}}^2$  and  $\chi_{\text{DESI}}^2$  surfaces across the  $(w_0, w_a)$  plane, each DESI-optimized. The two surfaces have opposite gradients: moving toward better BAOtr agreement (upper-left, more negative  $w_0$ ) worsens the DESI fit, and vice versa.

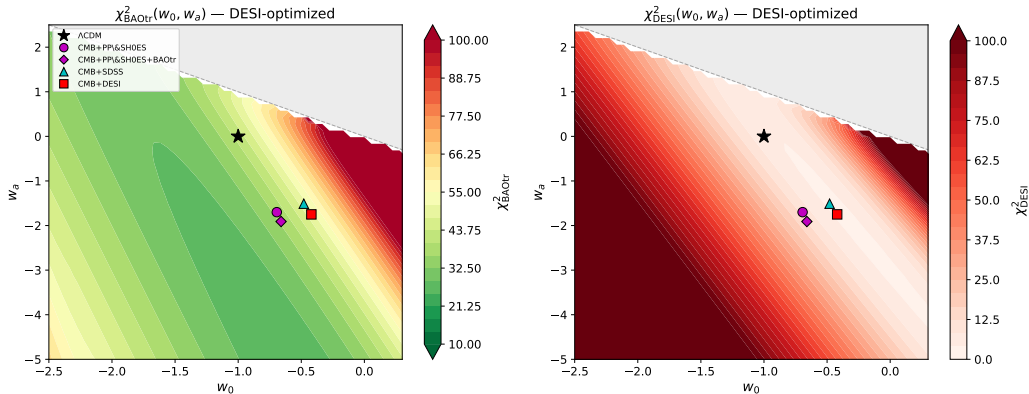


Figure 3: **Left:**  $\chi_{\text{BAOtr}}^2(w_0, w_a)$  (Method A, DESI-optimized). Green: low tension. **Right:**  $\chi_{\text{DESI}}^2(w_0, w_a)$ . Light: low  $\chi^2$ . The two surfaces have opposite gradients, confirming the trade-off. Symbols mark published posteriors as in Fig. 2.

### Why CPL cannot resolve the tension

The failure has a transparent origin. BAOtr prefers smaller  $D_M/r_d$  than DESI at  $z \lesssim 0.65$ . To fit BAOtr, the model needs smaller  $D_M/r_d$  at these redshifts, achieved by increasing  $H_0$  (since  $D_M \propto c/H_0$ ). But the  $\theta_*$  constraint links  $H_0$  to  $\Omega_m$ : increasing  $H_0$  requires decreasing  $\Omega_m$ , which changes  $E(z)$  and worsens the DESI fit. The direct clash at  $z = 0.510$  ( $3.7\sigma$ , data-versus-data) is the most acute manifestation: both datasets measure the same physical distance at the same redshift, so no modification of  $D_M(z)$  can reconcile them.

### 5.3. Robustness tests

#### Extrapolation and BGS anchor (Method B)

Table 8 presents the  $\Lambda\text{CDM}$  baseline  $\chi_B^2$  for six configurations of Method B.

Table 8: Method B  $\Lambda\text{CDM}$  baseline tension ( $\chi_B^2$  for 15 BAOtr points) under three extrapolation schemes, all including the BGS anchor at  $z = 0.295$ .  $\chi_B^2/N \geq 3.3$  in all cases.

Extrapolation	$\chi_B^2$	$\chi_B^2/N_{\text{pts}}$
Constant- $\alpha$ (default)	51.5	3.43
Model ( $\alpha = 1$ )	51.1	3.41
Linear	50.8	3.39

The three extrapolation schemes give  $\chi_B^2 = 50.8\text{--}51.5$  (spread  $\Delta\chi^2 = 0.7$ ), much smaller than the baseline tension itself. The dominant contributions ( $z = 0.35\text{--}0.65$ ) lie within the interpolation range and are unaffected by the extrapolation choice.

### *SDSS vs DESI*

Under Method B with SDSS anchors, the  $\Lambda$ CDM tension is  $\chi_B^2 = 39.9$  ( $H_0 = 68.0 \text{ km s}^{-1} \text{ Mpc}^{-1}$ ), somewhat lower than the DESI value of 51.5 but still highly significant ( $\chi^2/N = 2.7, 3.3\sigma$ ). The per-point pattern is strikingly similar (Fig. 4): all tensions negative, concentrated at  $z = 0.35\text{--}0.60$ , dominated by the same redshift bins. The persistence across two independent surveys rules out DESI-specific artefacts.

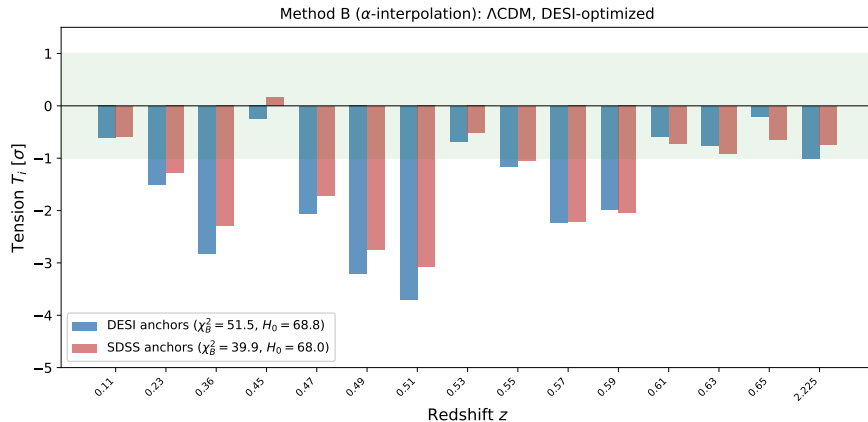


Figure 4: Per-point tension  $T_i$  (Method B,  $\Lambda$ CDM) using DESI anchors (blue) and SDSS anchors (red). Both produce the same pattern. The tension is a generic feature of the BAOtr–BAO 3D comparison.

### *5.4. Consistency between methods*

Figure 5 illustrates why the two methods give different  $\chi^2$  values but the same conclusion.

Under Method A (left panel), the CMB+DESI CPL model passes through the DESI data (as intended by the DESI optimization), but its lower  $H_0 = 63.8$  increases all distances, placing the curve above BAOtr. Under Method B (right panel), the  $\alpha$ -warping forces both models through DESI, but CPL’s smaller  $(D_M/r_d)^{\mathcal{M}}$  at the anchors inflates  $\alpha_j > 1$ , pushing the interpolated prediction above  $\Lambda$ CDM.

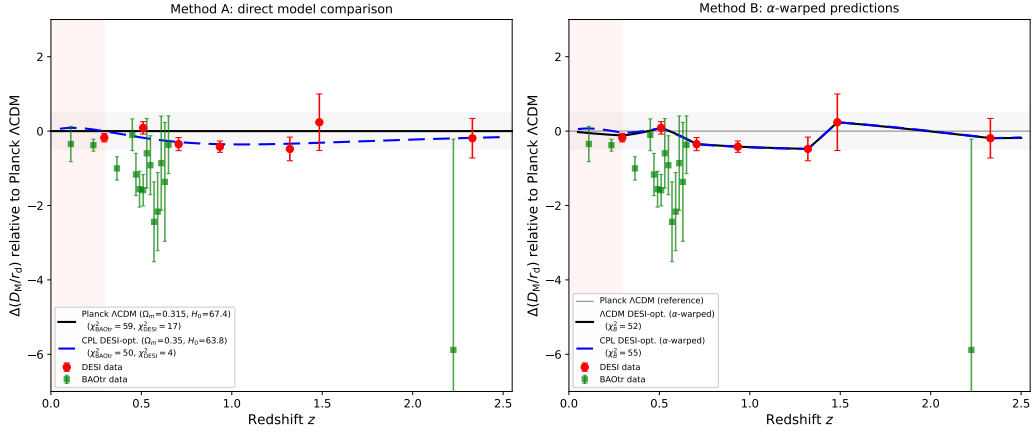


Figure 5: Residuals  $\Delta(D_M/r_d)$  relative to Planck  $\Lambda$ CDM ( $\Omega_m = 0.3153$ ,  $H_0 = 67.36 \text{ km s}^{-1} \text{ Mpc}^{-1}$ ). DESI data (red circles) and BAOtr data (green squares) are shown with their  $1\sigma$  uncertainties. The pink shaded region ( $z < 0.295$ ) marks the zone below the lowest DESI anchor, where Method B predictions depend on the extrapolation scheme. **Left (Method A):** Planck  $\Lambda$ CDM defines the zero line (black solid;  $\chi_{\text{BAOtr}}^2 = 59$ ,  $\chi_{\text{DESI}}^2 = 17$ ). The DESI-optimized CPL model ( $\Omega_m = 0.35$ ,  $H_0 = 63.8$ ; blue dashed) sits slightly below Planck  $\Lambda$ CDM at  $z \lesssim 1$  but cannot bridge the gap to BAOtr ( $\chi_{\text{BAOtr}}^2 = 50$ ,  $\chi_{\text{DESI}}^2 = 4$ ). **Right (Method B):**  $\alpha$ -warped predictions using DESI-optimized parameters, shown as residuals relative to Planck  $\Lambda$ CDM. The grey horizontal line marks the Planck  $\Lambda$ CDM reference. The DESI-optimized  $\Lambda$ CDM prediction (black solid;  $\chi_B^2 = 52$ ) and the CPL prediction (blue dashed;  $\chi_B^2 = 55$ ) are both pinned near zero at the DESI anchor redshifts by construction, but BAOtr remains 1–3 units below. In both panels, no model approaches the BAOtr data at  $z = 0.35\text{--}0.65$ .

Both perspectives confirm the same conclusion:

- Method A reveals the tension as a *dataset incompatibility*: no CPL model achieves low  $\chi^2$  for both DESI and BAOtr (Fig. 2).
- Method B reveals the tension as an *interpolation failure*: anchoring to DESI and varying the CPL backbone cannot bring the predictions into agreement with BAOtr.

## 6. Discussion

### 6.1. Fiducial independence and the rescaling error

The fiducial independence of published 3D BAO distances (Section 2.1) is a straightforward algebraic identity:  $\alpha_\perp$  is defined as the ratio of true to fiducial distances (Eq. 4), and the pipeline publishes  $\alpha_\perp \times D_M^{\text{fid}}/r_d^{\text{fid}}$ , in which the fiducial cancels by construction (Eq. 6). Residual effects are  $\delta\alpha/\alpha \lesssim 0.1\text{--}0.3\%$  [11, 41], two orders of magnitude below the BAOtr uncertainties. The rescaling approach overcorrects by a factor of 20–50 (Table 1), producing a spurious  $\Delta\chi^2 \sim 40\text{--}50$ .

### 6.2. Remaining explanations for the tension

With fiducial misspecification ruled out and CPL unable to reconcile the datasets (Section 5.2), two explanations remain.

#### *BAOtr systematics*

Projection effects from finite shell width can shift  $\theta_{\text{BAO}}$  at the  $\sim 0.5\text{--}1\%$  level per bin [28, 55, 56]; photometric redshift errors amplify these biases [57, 58]. All 15 measurements share the SDSS footprint and its angular systematics [58, 59, 60]: a coherent multiplicative systematic would bias all bins in the same direction, producing the observed one-signed offset. If confirmed, the BAOtr-inclusive CPL posteriors of Xu et al. [22] — showing strong Bayesian evidence for dynamical dark energy — would be unreliable, and the DESI-only results (which are inconclusive) would be the more trustworthy constraints.

#### *3D BAO systematics*

The DESI–SDSS consistency (Section 5.3) argues strongly against this: both independent surveys give the same tension pattern. Only a shared theoretical assumption could affect both identically.

*New physics beyond CPL*

Models with non-smooth  $w(z)$  —  $\Lambda_s$ CDM [34, 35, 36, 69, 70, 71], omnipotent dark energy [37], phantom-crossing scenarios [38, 39, 72, 73, 74], or reconstructed scalar-tensor gravity [75] — could produce distance features inaccessible to CPL. However, the direct  $z = 0.510$  clash ( $3.7\sigma$  data-versus-data;  $3.3\sigma$  against the best-fit  $\Lambda$ CDM prediction) cannot be resolved by modifying  $D_M(z)$ , since both datasets measure the same physical distance at the same redshift.<sup>2</sup> The model comparison alone contributes  $\chi^2 \approx 11$  to the Method A statistic, setting an irreducible floor.

Table 9 summarises the three categories.

Table 9: Remaining explanations for the BAOtr–BAO 3D tension.

Explanation	Key evidence	Discriminating test
BAOtr systematics	One-signed offset; shared SDSS footprint; $z = 0.510$ direct clash	Angular BAO from DESI; DES/Euclid/LSST photometric BAO
3D BAO systematics	DESI–SDSS consistency argues against	Alternative broadband parametrisations; blind mismatched-fiducial tests
New physics beyond CPL	Cannot resolve $z = 0.510$ clash; could help at other $z$	Fit $\Lambda_s$ CDM and other models to combined data

Of the three, BAOtr systematics are the most plausible given the current evidence.

*6.3. Connection to the Hubble tension*

The BAOtr–BAO 3D tension is directly connected to the Hubble tension. BAO measurements constrain  $r_d H_0$  through  $D_M(z)/r_d$ ; a dataset that prefers smaller  $D_M/r_d$  at low redshift (BAOtr) requires larger  $H_0$  at fixed  $r_d$ . Table 10 shows this bifurcation.

The anti-correlation is clear: CMB+DESI yields  $H_0 \approx 64$  with  $\chi^2_{\text{BAOtr}} = 49.8$ , while CMB+PP&SH0ES yields  $H_0 \approx 71$  with  $\chi^2_{\text{BAOtr}} = 37.4$ . Within

<sup>2</sup>A caveat: the BAOtr shell has width  $\Delta z = 0.02$  while the DESI LRG1 bin covers  $0.4 < z < 0.6$ . If  $D_M(z)/r_d$  varies rapidly within this range, the effective redshifts could differ slightly. However, the required  $\sim 13\%$  change over  $\Delta z \sim 0.05$  is implausible for any smooth expansion history.

Table 10:  $H_0$  from different CMB+BAO combinations in CPL [22], with our  $\chi_{\text{BAOtr}}^2$  (Table 7).  $T_{H_0}$  is relative to  $H_0^{\text{local}} = 73.50 \pm 0.81$  [68]. The  $H_0$  values are from full MCMC [22];  $\chi_{\text{BAOtr}}^2$  uses our DESI-optimized procedure.

Dataset	$w_0$	$w_a$	$H_0$ [km s <sup>-1</sup> Mpc <sup>-1</sup> ]	$T_{H_0}$ [ $\sigma$ ]	$\chi_{\text{BAOtr}}^2$
$\Lambda$ CDM	-1.00	0.00	$67.31 \pm 0.49$	-6.6	41.6
CMB+SDSS	-0.48	-1.51	$63.6_{-2.5}^{+2.2}$	-4.2	49.7
CMB+DESI	-0.42	-1.75	$63.9 \pm 2.0$	-4.4	49.8
CMB+PP&SH0ES	-0.69	-1.70	$70.87 \pm 0.68$	-2.5	37.4
CMB+BAOtr	-0.80	-1.68	$73.4_{-3.8}^{+2.2}$	-0.03	—

CPL, reducing the BAOtr tension requires increasing  $H_0$  (smaller  $D_{\text{M}}/r_{\text{d}}$ ), which pushes toward the local value but worsens the DESI fit. No single CPL model satisfies both. This anti-correlation is a structural limitation of the two-parameter CPL ansatz [76, 77, 78, 79].

#### 6.4. Limitations

Our DESI-optimization procedure determines  $\Omega_m$  by minimising  $\chi_{\text{DESI}}^2$  at each  $(w_0, w_a)$  with  $H_0$  set by  $\theta_*$ . A full MCMC with Planck likelihoods would also adjust  $\Omega_b h^2$  and  $n_s$ , potentially shifting  $\Omega_m$  and  $H_0$ ; however, the close agreement between our parameters and those of Xu et al. (Table 5) confirms that the dominant degeneracy is captured.

The BAOtr measurements are treated as statistically independent despite sharing the SDSS angular systematics. Correlated systematics would reduce the effective degrees of freedom, weakening the quoted  $p$ -values, though even halving the effective dof leaves the tension significant.

Our analysis is restricted to CPL. Models with more than two dark-energy parameters or non-smooth  $w(z)$  could improve the fit at redshifts between the DESI anchors, but must confront the  $z = 0.510$  direct clash ( $\chi^2 \approx 11$ ), which sets a model-independent floor.

We use only  $D_{\text{M}}/r_{\text{d}}$  (and  $D_{\text{V}}/r_{\text{d}}$  for BGS), neglecting  $D_{\text{H}}/r_{\text{d}}$  and the intra-tracer correlations  $\rho(D_{\text{M}}/r_{\text{d}}, D_{\text{H}}/r_{\text{d}})$ . Including  $D_{\text{H}}/r_{\text{d}}$  would tighten the DESI constraints but would not affect the BAOtr comparison, which is sensitive only to  $D_{\text{M}}/r_{\text{d}}$ .

## 7. Conclusions

We have investigated whether the tension between the fiducial-independent BAOtr dataset and the 3D BAO measurements from DESI DR2 and SDSS-IV can be attributed to the  $\Lambda$ CDM fiducial or resolved within CPL. Our main conclusions are:

1. **Published 3D BAO distances are fiducial-independent; rescaling overcorrects.** The fiducial cancels identically in  $\alpha_{\perp} \times D_{\text{M}}^{\text{fid}}/r_{\text{d}}^{\text{fid}}$  (Eq. 6), with residual effects at  $\lesssim 0.3\%$ . Multiplying published distances by  $D_{\text{M}}^{\text{CPL}}/D_{\text{M}}^{\Lambda\text{CDM}}$  overcorrects by a factor of 20–50 (Table 1).
2. **No CMB-consistent CPL model fits both DESI and BAOtr.** Scanning the  $(w_0, w_a)$  plane with  $\Omega_m$  and  $H_0$  determined by the  $\theta_*$  constraint and DESI optimization, we find an inescapable trade-off: the best DESI-fitting models ( $\chi_{\text{DESI}}^2 \lesssim 5$ ) give  $\chi_{\text{BAOtr}}^2 \gtrsim 42$ , while reducing  $\chi_{\text{BAOtr}}^2$  to  $\sim 37$  requires  $\chi_{\text{DESI}}^2 \gtrsim 8$  (Fig. 2, Table 7).
3. **The  $z = 0.510$  bin sets an irreducible tension floor.** At this redshift, BAOtr gives  $D_{\text{M}}/r_{\text{d}} = 11.91 \pm 0.42$  while DESI measures  $13.59 \pm 0.17$  — a  $3.7\sigma$  data-versus-data clash. Even against the best-fit  $\Lambda$ CDM prediction of 13.29, the disagreement is  $3.3\sigma$ , contributing  $\chi^2 \approx 11$  to the total.
4. **The results are robust.** The tension persists across two analysis methods (direct comparison and  $\alpha$ -interpolation), three extrapolation schemes, and substitution of SDSS for DESI ( $\chi_B^2 = 39.9$ ,  $3.3\sigma$ ).
5. **The remaining explanations are BAOtr systematics (most likely) or new physics beyond CPL.** The one-signed offset, shared SDSS footprint, and direct  $z = 0.510$  clash favour a coherent systematic in the angular BAO measurements. New physics with non-smooth  $w(z)$  could contribute at redshifts where the datasets do not overlap, but cannot resolve the direct clash.

**Outlook.** The key next steps are:

- (a) Angular BAO analysis of DESI spectroscopic data, eliminating SDSS-specific systematics.
- (b) Independent angular BAO from DES [80], Euclid [81], and LSST [82].
- (c) Sub-percent reassessment of BAOtr projection effects, photometric-redshift biases, and angular systematics.

- (d) Beyond-CPL models ( $\Lambda_s$ CDM, omnipotent dark energy, modified gravity) fitted to combined BAOtr + DESI + CMB data.

The origin of the BAOtr–BAO 3D tension remains open. What our analysis establishes is that the fiducial cosmology is not the answer, and the CPL parametrisation cannot reconcile the two datasets.

### Data availability

The Python code to reproduce all figures and tables is publicly available at:

<https://github.com/ipantos/BAOtr-BAO-3D-tension>.

### Declaration of competing interest

The authors declare no competing interests.

### Acknowledgements

The authors acknowledge networking support and participation in the CosmoVerse network.

### References

- [1] D. J. Eisenstein, W. Hu, M. Tegmark, Cosmic complementarity:  $H_0$  and  $\Omega_m$  from combining CMB experiments and redshift surveys, *Astrophys. J.* 504 (1998) L57–L60. [arXiv:astro-ph/9805239](https://arxiv.org/abs/astro-ph/9805239), [doi:10.1086/311582](https://doi.org/10.1086/311582).
- [2] D. J. Eisenstein, et al., Detection of the baryon acoustic peak in the large-scale correlation function of SDSS luminous red galaxies, *Astrophys. J.* 633 (2005) 560–574. [arXiv:astro-ph/0501171](https://arxiv.org/abs/astro-ph/0501171), [doi:10.1086/466512](https://doi.org/10.1086/466512).
- [3] A. Meiksin, M. White, J. A. Peacock, Baryonic signatures in large-scale structure, *Mon. Not. Roy. Astron. Soc.* 304 (1999) 851–864. [arXiv:astro-ph/9812214](https://arxiv.org/abs/astro-ph/9812214), [doi:10.1046/j.1365-8711.1999.02369.x](https://doi.org/10.1046/j.1365-8711.1999.02369.x).
- [4] C. Blake, K. Glazebrook, Probing dark energy using baryonic oscillations in the galaxy power spectrum as a cosmological ruler, *Astrophys. J.* 594 (2003) 665–673. [arXiv:astro-ph/0301632](https://arxiv.org/abs/astro-ph/0301632), [doi:10.1086/376983](https://doi.org/10.1086/376983).

- [5] H.-J. Seo, D. J. Eisenstein, Probing dark energy with baryonic acoustic oscillations from future large galaxy redshift surveys, *Astrophys. J.* 598 (2003) 720–740. [arXiv:astro-ph/0307460](#), [doi:10.1086/379122](#).
- [6] S. Cole, et al., The 2dF Galaxy Redshift Survey: Power-spectrum analysis of the final dataset and cosmological implications, *Mon. Not. Roy. Astron. Soc.* 362 (2005) 505–534. [arXiv:astro-ph/0501174](#), [doi:10.1111/j.1365-2966.2005.09318.x](#).
- [7] S. Alam, et al., The clustering of galaxies in the completed SDSS-III Baryon Oscillation Spectroscopic Survey: cosmological analysis of the DR12 galaxy sample, *Mon. Not. Roy. Astron. Soc.* 470 (2017) 2617–2652. [arXiv:1607.03155](#), [doi:10.1093/mnras/stx721](#).
- [8] S. Alam, et al., Completed SDSS-IV extended Baryon Oscillation Spectroscopic Survey: Cosmological implications of two decades of spectroscopic surveys at the Apache Point Observatory, *Phys. Rev. D* 103 (2021) 083533. [arXiv:2007.08991](#), [doi:10.1103/PhysRevD.103.083533](#).
- [9] B. Abareshi, et al., Overview of the Instrumentation for the Dark Energy Spectroscopic Instrument, *Astron. J.* 164 (2022) 207. [arXiv:2205.10939](#), [doi:10.3847/1538-3881/ac882b](#).
- [10] A. G. Adame, et al., DESI 2024 VI: Cosmological Constraints from the Measurements of Baryon Acoustic Oscillations, *JCAP* 02 (2025) 021. [arXiv:2404.03002](#), [doi:10.1088/1475-7516/2025/02/021](#).
- [11] M. Abdul Karim, et al., DESI DR2 Results II: Measurements of Baryon Acoustic Oscillations and Cosmological Constraints, *Phys. Rev. D* 112 (2025) 083515. [arXiv:2503.14738](#), [doi:10.1103/tr6y-kpc6](#).
- [12] M. Chevallier, D. Polarski, Accelerating universes with scaling dark matter, *Int. J. Mod. Phys. D* 10 (2001) 213–224. [arXiv:gr-qc/0009008](#), [doi:10.1142/S0218271801000822](#).
- [13] E. V. Linder, Exploring the expansion history of the universe, *Phys. Rev. Lett.* 90 (2003) 091301. [arXiv:astro-ph/0208512](#), [doi:10.1103/PhysRevLett.90.091301](#).

- [14] N. Aghanim, et al., Planck 2018 results. VI. Cosmological parameters, *Astron. Astrophys.* 641 (2020) A6, [Erratum: *Astron. Astrophys.* 652 (2021) C4]. [arXiv:1807.06209](#), [doi:10.1051/0004-6361/201833910](#).
- [15] W. Giarè, M. Najafi, S. Pan, E. Di Valentino, J. T. Firouzjaee, Robust Preference for Dynamical Dark Energy in DESI BAO and SN Measurements, *JCAP* 10 (2024) 035. [arXiv:2407.16689](#), [doi:10.1088/1475-7516/2024/10/035](#).
- [16] M. Cortès, A. R. Liddle, Interpreting DESI’s evidence for evolving dark energy, *JCAP* 12 (2024) 007. [arXiv:2404.08056](#), [doi:10.1088/1475-7516/2024/12/007](#).
- [17] W. J. Wolf, C. García-García, D. J. Bartlett, P. G. Ferreira, Scant evidence for thawing quintessence, *Phys. Rev. D* 110 (2024) 083528. [arXiv:2408.17318](#), [doi:10.1103/PhysRevD.110.083528](#).
- [18] W. Giarè, Dynamical Dark Energy Beyond Planck? Constraints from multiple CMB probes, DESI BAO and Type-Ia Supernovae, *Phys. Rev. D* 112 (2025) 023508. [arXiv:2409.17074](#), [doi:10.1103/ss37-cxhn](#).
- [19] L. Perivolaropoulos, F. Skara, Challenges for  $\Lambda$ CDM – An update, *New Astron. Rev.* 95 (2022) 101659. [arXiv:2105.05208](#), [doi:10.1016/j.newar.2022.101659](#).
- [20] I. Pantos, L. Perivolaropoulos, Status of the  $S_8$  Tension: A 2026 Review of Probe Discrepancies, *Phys. Dark Univ.* (2026). [arXiv:2602.12238](#).
- [21] C. G. Tsagas, L. Perivolaropoulos, K. Asvesta, Large-scale peculiar velocities in the universe, *Phys. Rep.* To appear (2025). [arXiv:2510.05340](#).
- [22] T. Xu, S. Kumar, Y. Chen, A. J. S. Capistrano, Ö. Akarsu, Probing dynamical dark energy with late-time data: Evidence, tensions, and the limits of the  $w_0w_a$ CDM framework, *arXiv* (2026). [arXiv:2602.11936](#).
- [23] R. C. Nunes, S. K. Yadav, J. F. Jesus, A. Bernui, Cosmological parameter analyses using transversal BAO data, *Mon. Not. Roy. Astron. Soc.* 497 (2020) 2133–2141. [arXiv:2002.09293](#), [doi:10.1093/mnras/staa2036](#).

- [24] D. Scolnic, et al., The Pantheon+ Analysis: The Full Dataset and Light-Curve Release, *Astrophys. J.* 938 (2022) 113. [arXiv:2112.03863](#), [doi:10.3847/1538-4357/ac8b7a](#).
- [25] D. Brout, et al., The Pantheon+ Analysis: Cosmological Constraints, *Astrophys. J.* 938 (2022) 110. [arXiv:2202.04077](#), [doi:10.3847/1538-4357/ac8e04](#).
- [26] A. G. Riess, et al., A Comprehensive Measurement of the Local Value of the Hubble Constant with 1 km/s/Mpc Uncertainty from the Hubble Space Telescope and the SH0ES Team, *Astrophys. J. Lett.* 934 (2022) L7. [arXiv:2112.04510](#), [doi:10.3847/2041-8213/ac5c5b](#).
- [27] C. Alcock, B. Paczyński, An evolution free test for non-zero cosmological constant, *Nature* 281 (1979) 358. [doi:10.1038/281358a0](#).
- [28] E. Sánchez, A. Carnero, J. García-Bellido, E. Gaztañaga, F. de Simoni, M. Crocce, A. Cabré, P. Fosalba, D. Alonso, Tracing the sound horizon scale with photometric redshift surveys, *Mon. Not. Roy. Astron. Soc.* 411 (2011) 277–288. [arXiv:1006.3226](#), [doi:10.1111/j.1365-2966.2010.17679.x](#).
- [29] G. C. Carvalho, A. Bernui, M. Benetti, J. C. Carvalho, J. S. Alcaniz, Baryon Acoustic Oscillations from the SDSS DR10 galaxies angular correlation function, *Phys. Rev. D* 93 (2016) 023530. [arXiv:1507.08972](#), [doi:doi.org/10.1103/PhysRevD.93.023530](#).
- [30] G. C. Carvalho, A. Bernui, M. Benetti, J. C. Carvalho, E. de Carvalho, J. S. Alcaniz, Baryon acoustic oscillations from the SDSS DR10 galaxies angular correlation function, *Astropart. Phys.* 119 (2020) 102432. [arXiv:1709.00271](#), [doi:10.1016/j.astropartphys.2020.102432](#).
- [31] E. de Carvalho, A. Bernui, F. Avila, C. P. Novaes, J. P. Nogueira-Cavalcante, BAO angular scale at  $z_{\text{eff}} = 0.11$  with the SDSS blue galaxies, *Astron. Astrophys.* 649 (2021) A20. [arXiv:2103.14121](#), [doi:10.1051/0004-6361/202039936](#).
- [32] J. S. Alcaniz, G. C. Carvalho, A. Bernui, J. C. Carvalho, M. Benetti, Measuring baryon acoustic oscillations with angular two-point function, in: *Fundam. Theor. Phys.*, Vol. 187, Springer, 2017, pp. 11–19. [arXiv:1611.08458](#), [doi:10.1007/978-3-319-51700-1\\_2](#).

- [33] E. de Carvalho, A. Bernui, G. C. Carvalho, C. P. Novaes, H. S. Xavier, Angular Baryon Acoustic Oscillation measure at  $z = 2.225$  from the SDSS quasar survey, JCAP 04 (2018) 064. [arXiv:1709.00113](#), [doi:10.1088/1475-7516/2018/04/064](#).
- [34] Ö. Akarsu, J. D. Barrow, L. A. Escamilla, J. A. Vazquez, Graduated dark energy: Observational hints of a spontaneous sign switching of the cosmological constant, Phys. Rev. D 101 (2020) 063528. [arXiv:1912.08751](#), [doi:10.1103/PhysRevD.101.063528](#).
- [35] Ö. Akarsu, S. Kumar, E. Özülker, J. A. Vazquez, Relaxing cosmological tensions with a sign switching cosmological constant, Phys. Rev. D 104 (2021) 123512. [arXiv:2108.09239](#), [doi:10.1103/PhysRevD.108.023513](#).
- [36] Ö. Akarsu, S. Kumar, E. Özülker, J. A. Vazquez, A. Yadav, Relaxing cosmological tensions with a sign switching cosmological constant: Improved results with Planck, BAO, and Pantheon data, Phys. Rev. D 108 (2023) 023513. [arXiv:2211.05742](#), [doi:10.1103/PhysRevD.108.023513](#).
- [37] S. A. Adil, Ö. Akarsu, E. Di Valentino, R. C. Nunes, E. Özülker, A. A. Sen, E. Specogna, Omnipotent dark energy: A phenomenological answer to the Hubble tension, Phys. Rev. D 109 (2024) 023527. [arXiv:2306.08046](#), [doi:10.1103/PhysRevD.109.023527](#).
- [38] E. Di Valentino, A. Mukherjee, A. A. Sen, Dark Energy with Phantom Crossing and the  $H_0$  Tension, Entropy 23 (2021) 404. [arXiv:2005.12587](#), [doi:10.3390/e23040404](#).
- [39] L. A. Escamilla, Ö. Akarsu, E. Di Valentino, J. A. Vazquez, Model-independent reconstruction of the Interacting Dark Energy Kernel: Binned and Gaussian process, JCAP 11 (2023) 051. [arXiv:2305.16290](#), [doi:10.1088/1475-7516/2023/11/051](#).
- [40] V. Sahni, Y. Shtanov, Braneworld models of dark energy, JCAP 11 (2003) 014. [arXiv:astro-ph/0202346](#), [doi:10.1088/1475-7516/2003/11/014](#).

- [41] A. Pérez-Fernández, et al., Fiducial-Cosmology-dependent systematics for the DESI 2024 BAO Analysis, JCAP 01 (2025) 141. [arXiv:2406.06085](#), [doi:10.1088/1475-7516/2025/01/141](#).
- [42] D. Pedrotti, L. A. Escamilla, V. Marra, L. Perivolaropoulos, S. Vagnozzi, BAO miscalibration cannot rescue late-time solutions to the Hubble tension, Phys. Rev. D (2025). [arXiv:2510.01974](#), [doi:10.1103/pn9j-8whx](#).
- [43] S. D. Landy, A. S. Szalay, Bias and variance of angular correlation functions, Astrophys. J. 412 (1993) 64–71. [doi:10.1086/172900](#).
- [44] D. J. Eisenstein, H.-J. Seo, E. Sirko, D. N. Spergel, Improving Cosmological Distance Measurements by Reconstruction of the Baryon Acoustic Peak, Astrophys. J. 664 (2007) 675–679. [arXiv:astro-ph/0604362](#), [doi:10.1086/518712](#).
- [45] N. Padmanabhan, X. Xu, D. J. Eisenstein, R. Scalzo, A. J. Cuesta, K. T. Mehta, E. Kazin, A 2 per cent distance to  $z = 0.35$  by reconstructing baryon acoustic oscillations — I. Methods and application to the Sloan Digital Sky Survey, Mon. Not. Roy. Astron. Soc. 427 (2012) 2132–2145. [arXiv:1202.0090](#), [doi:10.1111/j.1365-2966.2012.21888.x](#).
- [46] X. Xu, N. Padmanabhan, D. J. Eisenstein, K. T. Mehta, A. J. Cuesta, A 2 per cent distance to  $z = 0.35$  by reconstructing baryon acoustic oscillations — II: Fitting techniques, Mon. Not. Roy. Astron. Soc. 427 (2012) 2146–2167. [arXiv:1202.0091](#), [doi:10.1111/j.1365-2966.2012.21573.x](#).
- [47] L. Anderson, et al., The clustering of galaxies in the SDSS-III Baryon Oscillation Spectroscopic Survey: baryon acoustic oscillations in the Data Releases 10 and 11 Galaxy samples, Mon. Not. Roy. Astron. Soc. 441 (2014) 24–62. [arXiv:1312.4877](#), [doi:10.1093/mnras/stw2373](#).
- [48] F. Beutler, H.-J. Seo, S. Saito, C.-H. Chuang, A. J. Cuesta, D. J. Eisenstein, H. Gil-Marín, J. N. Grieb, N. Hand, F.-S. Kitaura, C. Modi, T. Nishimichi, M. Olmstead, F. Prada, A. J. Ross, R. Scoccimarro, E. Sefusatti, A. Slosar, J. Tinker, R. Tojeiro, M. Vargas-Magaña, The clustering of galaxies in the completed SDSS-III Baryon Oscillation Spectroscopic Survey: baryon acoustic oscillations in the Fourier space,

- Mon. Not. Roy. Astron. Soc. 464 (2017) 3409–3430. [arXiv:1607.03149](#), [doi:10.1093/mnras/stw2373](#).
- [49] A. J. Ross, et al., The clustering of galaxies in the completed SDSS-III Baryon Oscillation Spectroscopic Survey: observational systematics and baryon acoustic oscillations in the correlation function, Mon. Not. Roy. Astron. Soc. 464 (2017) 1168–1191. [arXiv:1607.03145](#), [doi:10.1093/mnras/stw2372](#).
- [50] V. Poulin, T. L. Smith, T. Karwal, M. Kamionkowski, Early Dark Energy Can Resolve The Hubble Tension, Phys. Rev. Lett. 122 (2019) 221301. [arXiv:1811.04083](#), [doi:10.1103/PhysRevLett.122.221301](#).
- [51] T. Karwal, M. Kamionkowski, Dark energy at early times, the Hubble parameter, and the string axiverse, Phys. Rev. D 94 (2016) 103523. [arXiv:1608.01309](#), [doi:10.1103/PhysRevD.94.103523](#).
- [52] A. G. Adame, et al., DESI 2024 III: Baryon Acoustic Oscillations from Galaxies and Quasars, JCAP 04 (2025) 012. [arXiv:2404.03000](#), [doi:10.1088/1475-7516/2025/04/012](#).
- [53] A. Carnero, E. Sánchez, M. Crocce, A. Cabré, E. Gaztañaga, Clustering of photometric luminous red galaxies — II. Cosmological implications from the baryon acoustic scale, Mon. Not. Roy. Astron. Soc. 419 (2012) 1689–1694. [arXiv:1104.5426](#), [doi:10.1111/j.1365-2966.2011.19832.x](#).
- [54] E. Sánchez, D. Alonso, F. J. Sánchez, J. García-Bellido, I. Sevilla, Precise measurement of the radial baryon acoustic oscillation scales in galaxy redshift surveys, Mon. Not. Roy. Astron. Soc. 434 (2013) 2008–2019. [arXiv:1210.6446](#), [doi:10.1093/mnras/stt1146](#).
- [55] T. Nishimichi, et al., Characteristic scales of baryon acoustic oscillations from perturbation theory: non-linearity and redshift-space distortion effects, Publ. Astron. Soc. Jap. 59 (2007) 1049–1060. [arXiv:0705.1589](#), [doi:10.1093/pasj/59.6.1049](#).
- [56] M. Crocce, A. Cabré, E. Gaztañaga, Modelling the angular correlation function and its full covariance in photometric galaxy surveys, Mon. Not. Roy. Astron. Soc. 414 (2011) 329–349. [arXiv:1004.4640](#), [doi:10.1111/j.1365-2966.2011.18393.x](#).

- [57] N. Padmanabhan, et al., Calibrating photometric redshifts of luminous red galaxies, *Mon. Not. Roy. Astron. Soc.* 378 (2007) 852–872. [arXiv:astro-ph/0703454](#), [doi:10.1111/j.1365-2966.2007.11593.x](#).
- [58] A. J. Ross, W. J. Percival, M. Crocce, A. Cabré, E. Gaztañaga, Measuring redshift-space distortions using photometric surveys, *Mon. Not. Roy. Astron. Soc.* 417 (2011) 1350–1373. [arXiv:1102.0968](#), [doi:10.1111/j.1365-2966.2011.19351.x](#).
- [59] S. Ho, A. Cuesta, H.-J. Seo, et al., Clustering of Sloan Digital Sky Survey III Photometric Luminous Galaxies: The Measurement, Systematics, and Cosmological Implications, *Astrophys. J.* 761 (2012) 14. [arXiv:1201.2137](#), [doi:10.1088/0004-637X/761/1/14](#).
- [60] B. Leistedt, H. V. Peiris, Exploiting the full potential of photometric quasar surveys: optimal power spectra through blind mitigation of systematics, *Mon. Not. Roy. Astron. Soc.* 444 (2014) 2. [arXiv:1404.6530](#), [doi:10.1093/mnras/stu1439](#).
- [61] A. J. Ross, L. Samushia, C. Howlett, W. J. Percival, A. Burden, M. Manera, The clustering of the SDSS DR7 main Galaxy sample — I. A 4 per cent distance measure at  $z = 0.15$ , *Mon. Not. Roy. Astron. Soc.* 449 (2015) 835–847. [arXiv:1409.3242](#), [doi:10.1093/mnras/stv154](#).
- [62] J. E. Bautista, et al., The completed SDSS-IV extended Baryon Oscillation Spectroscopic Survey: measurement of the BAO and growth rate of structure of the luminous red galaxy sample from the anisotropic correlation function between redshifts 0.6 and 1.0, *Mon. Not. Roy. Astron. Soc.* 500 (2021) 736–762. [arXiv:2007.08993](#), [doi:10.1093/mnras/staa2800](#).
- [63] H. Gil-Marín, et al., The completed SDSS-IV extended Baryon Oscillation Spectroscopic Survey: measurement of the BAO and growth rate of structure of the luminous red galaxy sample from the anisotropic power spectrum between redshifts 0.6 and 1.0, *Mon. Not. Roy. Astron. Soc.* 498 (2020) 2492–2531. [arXiv:2007.08994](#), [doi:10.1093/mnras/staa2455](#).
- [64] A. de Mattia, et al., The completed SDSS-IV extended Baryon Oscillation Spectroscopic Survey: measurement of the BAO and growth rate of structure of the emission line galaxy sample from the anisotropic power

- spectrum between redshifts 0.6 and 1.1, *Mon. Not. Roy. Astron. Soc.* 501 (2021) 5616–5645. [arXiv:2007.09008](#), [doi:10.1093/mnras/staa3891](#).
- [65] R. Neveux, et al., The completed SDSS-IV extended Baryon Oscillation Spectroscopic Survey: BAO and RSD measurements from the anisotropic power spectrum of the quasar sample between redshift 0.8 and 2.2, *Mon. Not. Roy. Astron. Soc.* 499 (2020) 210–229. [arXiv:2007.08999](#), [doi:10.1093/mnras/staa2780](#).
- [66] J. Hou, et al., The completed SDSS-IV extended Baryon Oscillation Spectroscopic Survey: BAO and RSD measurements from anisotropic clustering analysis of the quasar sample in configuration space between redshift 0.8 and 2.2, *Mon. Not. Roy. Astron. Soc.* 500 (2021) 1201–1221. [arXiv:2007.08998](#), [doi:10.1093/mnras/staa3234](#).
- [67] H. du Mas des Bourboux, et al., The completed SDSS-IV extended Baryon Oscillation Spectroscopic Survey: baryon acoustic oscillations with Lyman- $\alpha$  forests, *Astrophys. J.* 901 (2020) 153. [arXiv:2007.08995](#), [doi:10.3847/1538-4357/abb085](#).
- [68] S. Casertano, et al., The Local Distance Network: a community consensus report on the measurement of the Hubble constant at 1% precision, *Astron. Astrophys.* (2025). [arXiv:2510.23823](#), [doi:10.1051/0004-6361/202557993](#).
- [69] N. Menci, S. A. Adil, U. Mukhopadhyay, A. A. Sen, S. Vagnozzi, Negative cosmological constant in the dark energy sector: tests from JWST photometric and spectroscopic observations of high-redshift galaxies, *JCAP* 07 (2024) 072. [arXiv:2401.12659](#), [doi:10.1088/1475-7516/2024/07/072](#).
- [70] O. Akarsu, M. Eingorn, L. Perivolaropoulos, A. E. Yükselci, A. Zhuk, Dynamical dark energy with AdS-dS transitions vs. Baryon Acoustic Oscillations at  $z = 2.3$ – $2.4$ , *arXiv* (2025). [arXiv:2504.07299](#).
- [71] Ö. Akarsu, E. Di Valentino, S. Kumar, R. C. Nunes, E. Özüiker, J. A. Vazquez,  $\Lambda_s$ CDM cosmology from DESI 2024 and beyond: no sign of dark energy metamorphosis, *arXiv:2412.00965* (2024). [arXiv:2412.00965](#).

- [72] G. Alestas, L. Kazantzidis, L. Perivolaropoulos,  $H_0$  tension, phantom dark energy and cosmological parameter degeneracies, Phys. Rev. D 101 (2020) 123516. [arXiv:2004.08363](#), [doi:10.1103/PhysRevD.101.123516](#).
- [73] G. Alestas, L. Perivolaropoulos, Late-time approaches to the Hubble tension deforming  $H(z)$ , worsen the growth tension, Mon. Not. Roy. Astron. Soc. 504 (2021) 3956–3962. [arXiv:2012.13932](#), [doi:10.1093/mnras/stab1070](#).
- [74] V. Marra, L. Perivolaropoulos, Rapid transition of  $G_{\text{eff}}$  at  $z_t \simeq 0.01$  as a possible solution of the Hubble and growth tensions, Phys. Rev. D 104 (2021) L021303. [arXiv:2102.06012](#), [doi:10.1103/PhysRevD.104.L021303](#).
- [75] D. Efstratiou, E. A. Paraskevas, L. Perivolaropoulos, Addressing the DESI DR2 Phantom-Crossing Anomaly and Enhanced  $H_0$  Tension with Reconstructed Scalar-Tensor Gravity, arXiv (11 2025). [arXiv:2511.04610](#).
- [76] S. Vagnozzi, Seven Hints That Early-Time New Physics Alone Is Not Sufficient to Solve the Hubble Tension, Universe 9 (9) (2023) 393. [arXiv:2308.16628](#), [doi:10.3390/universe9090393](#).
- [77] S. Vagnozzi, F. Pacucci, A. Loeb, Implications for the Hubble tension from the ages of the oldest astrophysical objects, JHEAp 36 (2022) 27–35. [arXiv:2105.10421](#), [doi:10.1016/j.jheap.2022.07.004](#).
- [78] I. Pantos, L. Perivolaropoulos, Dissecting the Hubble tension: Insights from a diverse set of Sound Horizon-free  $H_0$  measurements, arXiv (1 2026). [arXiv:2601.00650](#).
- [79] D. Pedrotti, J.-Q. Jiang, L. A. Escamilla, S. S. da Costa, S. Vagnozzi, Multidimensionality of the Hubble tension: The roles of  $\Omega_m$  and  $\omega_c$ , Phys. Rev. D 111 (2) (2025) 023506. [arXiv:2408.04530](#), [doi:10.1103/PhysRevD.111.023506](#).
- [80] T. M. C. Abbott, et al., Dark Energy Survey Year 3 results: A 2.7% measurement of baryon acoustic oscillation distance scale at redshift 0.835, Phys. Rev. D 105 (2022) 043512. [arXiv:2107.04646](#), [doi:10.1103/PhysRevD.105.043512](#).

- [81] Y. Mellier, et al., Euclid. I. Overview of the Euclid mission, *Astron. Astrophys.* 697 (2025) A1. [arXiv:2405.13491](https://arxiv.org/abs/2405.13491), [doi:10.1051/0004-6361/202450810](https://doi.org/10.1051/0004-6361/202450810).
- [82] Ž. Ivezić, et al., LSST: from Science Drivers to Reference Design and Anticipated Data Products, *Astrophys. J.* 873 (2019) 111. [arXiv:0805.2366](https://arxiv.org/abs/0805.2366), [doi:10.3847/1538-4357/ab042c](https://doi.org/10.3847/1538-4357/ab042c).